nature cancer

Article

https://doi.org/10.1038/s43018-026-01177-4

Copper depletion boosts CNS leukemia therapy by inhibiting nucleotide synthesis through impairment of mitochondrial complex IV activity

Received: 18 June 2025

Accepted: 23 April 2026

Published online: 25 May 2026

Check for updates

Alan Y. L. Wong[1,2,3,4], Jacob W. Myers[3], Gyan Prakash[5], Alice Ma[3], Jeannette R. Brook[3], Boryana Petrova[3,6], Baran Bulut[2,3], Ralph White III[7], Catherine Merz[3], Maeve de Souza[3], Adam G. Maynard[3,4], Peng Wang[2,3,4], Amy Yu[3,4], Nancy K. Pohl[3,8], Michal Weitman[3], Lewis B. Silverman[9], Kimberly Stegmaier[9], L. Stirling Churchman[5], Peter D. Cole[10], Donita C. Brady[7,11] & Naama Kanarek[2,3,4] ✉

The nutrient-sparse cerebrospinal fluid (CSF) poses a major challenge to spreading cancer cells. Despite this challenge, leukemia cells spread to the CSF, requiring aggressive central nervous system (CNS)-directed treatment that can lead to neurotoxicity. Here we used a targeted in vivo CRISPR screen to identify nutritional dependencies of systemic and CNS acute lymphoblastic leukemia (ALL). We show that copper depletion, either by genetic deletion of the transporter *SLC31A1* or by dietary intervention, slows the growth of both systemic and CNS leukemia in a xenograft model. Mechanistically, copper depletion inhibits complex IV and nucleotide synthesis to slow the growth of leukemia cells. Furthermore, dietary depletion of copper combined with the standard-of-care therapy methotrexate inhibits leukemia progression in cell-line-derived and patient-derived xenograft models. Our findings identify copper as an actionable micronutrient to disrupt nucleotide synthesis in ALL and proposes copper depletion as a way to boost leukemia therapy in the hard-to-treat CNS.

Spread of cancer into the cerebrospinal fluid (CSF) is a deadly complication in both solid and liquid tumors[1,2]. In the case of acute lymphoblastic leukemia (ALL), the most common childhood cancer, prophylactic therapy delivered to the CSF is necessary to prevent spread of the cancer and to achieve long-term remission[3]. However, CSF-directed treatments can become ineffective[4], leading to relapse. In addition, central nervous system (CNS)-directed treatment contributes to the risk of long-term cognitive deficits in survivors[5]. The antifolate drug methotrexate (MTX) is a cornerstone of both systemic and CNS ALL therapy[6] and restrains leukemic growth by inhibiting purine and pyrimidine synthesis[7]; however, MTX treatment is linked to acute neurotoxicity, leukoencephalopathy and the potential for long-term neurological complications[8,9]. Even with excellent 5-year and 10-year survival rates in pediatric ALL, there is still a critical need to improve survivorship. A better mechanistic understanding of MTX-induced neurotoxicity[10,11] can inform strategies to reduce MTX-induced neurotoxicity. Novel therapies that target cancer-specific vulnerabilities while sparing healthy brain tissue can further improve outcomes and the quality of life of survivors.

The CSF is nutrient sparse compared to the blood[12] and yet cancer cells are able to spread into and grow in this metabolically unfavorable environment[1,13]. Cancer cells often rewire their metabolism to adapt to nutritional constraints and, in some cases, these adaptations

A full list of affiliations appears at the end of the paper. ✉e-mail: naama.kanarek@childrens.harvard.edu

create therapeutic vulnerabilities[14–16]. Motivated by the need to identify ALL-specific vulnerabilities in the CNS milieu, we asked whether nutritional adaptation of leukemia cells to the CSF creates metabolic dependencies that can be targeted therapeutically. Therefore, we undertook a targeted in vivo CRISPR screen in a xenograft mouse model of ALL. This screen identified genes involved in copper metabolism and oxidative phosphorylation (*SLC31A1*, *SDHA* and *GSR*) as therapeutic vulnerabilities in ALL cells. We found that, in leukemia cells, copper ions primarily support electron transport chain (ETC) activity. Using mechanistic rescue experiments and metabolite profiling, we show that copper depletion restrains nucleotide synthesis to compromise leukemia cell proliferation. Lastly, we validated the therapeutic potential of combining copper depletion with MTX, a core ALL therapy, to reduce systemic and CNS disease in a xenograft model of ALL.

Results

In vivo CRISPR screen identifies copper metabolism as a dependency in ALL

For our CRISPR screen, we used the SEM cell line, a human ALL cell line driven by the high-risk t(4;11) *KMT2A–AFF1* translocation[17]. This cell line readily spreads to the CNS when engrafted in immunodeficient mice[15]. As the engraftment efficiency of cells greatly limits the single-guide RNA (sgRNA) coverage in in vivo screens[18], a genome-wide screen becomes practically challenging. To determine how many cells survive the engraftment process and could be represented in an in vivo CRISPR screen in our model, we first used a genetic barcoding approach (Extended Data Fig. 1a). This approach revealed variable recovery of barcodes across organs, with millions of cells recovered from the leptomeninges at the experimental endpoint (Extended Data Fig. 1b) emerging from only ~196 clones (Extended Data Fig. 1c and Supplementary Table 1). Of note, some barcodes remained unique to the leptomeninges (Extended Data Fig. 1d). Given the low engraftment efficiency in our model, we determined that an in vivo screen using four gRNAs per gene would allow for roughly 40 genes to be screened per mouse while retaining sufficient coverage in the CNS. Therefore, to increase the total number of genes screened, we conducted four independent CRISPR screens in four independent cohorts of mice. Each CRISPR screen targeted 43 unique genes each, for a total of 172 genes. Each CRISPR library contained 172 unique sgRNAs targeting 43 metabolic genes, along with 20 identical control, intergenic sgRNAs and two sgRNAs targeting essential genes (*DHFR* and *DHODH*). These shared sgRNAs enabled us to compare the performance of each library (assessing for depletion of the sgRNAs targeting essential genes) and unify our analysis by normalizing our results to the intergenic sgRNAs (Extended Data Fig. 1e). Since the number of genes to be screened was limited, our gene list was not selected in an unbiased manner; instead, it was hand-curated and enriched for genes in metabolic pathways that were of interest to us and that we predicted to be important for cell survival in the metabolic environment of the CSF (Supplementary Table 2).

To conduct our CRISPR screen, SEM cells stably expressing Cas9–RFP were transduced with CRISPR library lentivirus encoding for sgRNAs under a vexGFP reporter. Transduced cells underwent fluorescence-activated cell sorting (FACS) and were engrafted into irradiated NOD-SCID mice (see Methods). At the humane endpoint, cells were harvested by rough dissection from the leptomeninges, spleen, bone marrow and blood and submitted for next-generation sequencing (NGS) (Fig. 1a and Supplementary Table 3).

sgRNAs targeting *CXCR4* were the most significantly depleted from all sites (Extended Data Fig. 1f), consistent with published data highlighting *CXCR4*'s role in regulating leukemia stem cell engraftment and regulating cell survival in ALL[19]. Additionally, sgRNAs targeting the de novo purine synthesis enzymes *GART*, *PAICS* and *ATIC* were also significantly depleted (Extended Data Fig. 1f), consistent with broad sensitivity of ALL cells to the nucleotide synthesis inhibitor and core ALL therapy methotrexate (MTX). Pairwise comparisons of the spleen, bone marrow and leptomeninges also revealed several organ-specific dependencies (Extended Data Fig. 1g).

Given the small number of genes in our screen, we looked for genes that scored significantly and are functionally linked. sgRNAs targeting the mammalian cell-surface copper transporter *SLC31A1* were depleted in all sites, along with sgRNAs targeting glutathione disulfide reductase (*GSR*) and succinate dehydrogenase complex flavoprotein subunit A (*SDHA*) (Fig. 1b). Together, these genes connect the import and intracellular chaperoning of copper ions[20] with a critical downstream function of copper–supporting ETC activity[21,22] (Fig. 1c). *SDHA* may be the only ETC gene that scored in our screen because other ETC genes are essential and likely to drop out during in vitro transduction without supplementation of uridine and pyruvate in the medium. Although loss of *SDHA* is functionally distinct from ETC inhibition due to copper deficiency, recent reports have implicated a role for *SDHA* in the regulation of purine synthesis[23], strengthening the connection between a dependency on ETC and nucleotide synthesis in ALL. Interestingly, we found CSF levels of copper in NOD-SCID mice to be significantly lower than levels in the plasma (Extended Data Fig. 2a), matching what is seen in humans[24], and raising the possibility that copper depletion might limit availability of an already scarce micronutrient. Notably, serum copper levels are increased in persons with leukemia[25,26] and in ALL blasts compared to normal lymphocytes[27]. Furthermore, relapse-fated ALL cells and CNS-derived ALL cells exhibit transcriptional and functional signatures of increased oxidative phosphorylation, suggesting an opportunity to target metabolic shifts associated with treatment resistance[28,29]. Our screen extends on these findings to suggest that inhibition of copper metabolism and oxidative phosphorylation can inhibit the growth of ALL in vivo.

To validate the importance of copper metabolism in SEM cells, we used a competitive mixing experiment in vivo[15] (Fig. 1d). FACS-purified *SLC31A1*-knockout (*SLC31A1*-KO) GFP (Extended Data Fig. 2b,c) or control GFP SEM cells were mixed with mCherry-expressing SEM cells, validated by flow cytometry (Supplementary Fig. 1a) and then engrafted into mice using either intravenous (i.v.) injection into the peripheral blood or intracisternal (i.c.) injection into the CSF. Here, i.v. injection primarily models a systemic disease in which the leukemia cells engraft in hematologic organs such as the spleen and the bone marrow and migrate to the CNS, whereas i.c. injection bypasses CNS-homing and results in primary CNS leukemia (Extended Data Fig. 2d,e). At the humane endpoint, mice were euthanized and cells were isolated from either the spleen or the leptomeninges for flow cytometry to determine the percentage of GFP-positive cells (Supplementary Fig. 1b,c).

When introduced i.v., SEM cells with KO of *SLC31A1* exhibited significantly reduced the growth in the spleen (Fig. 1e) and in the leptomeninges (Extended Data Fig. 2f) compared to control cells. To assess whether this effect is because of reduced engraftment, we repeated this mixing experiment using an sgRNA driven by a doxycycline-inducible promoter and administered doxycycline in the drinking water starting at day 5 after engraftment (Extended Data Fig. 2g,h). In this system, *SLC31A1*-KO cells still exhibited a growth defect compared to control cells in the spleen (Extended Data Fig. 2i), suggesting that negative selection against *SLC31A1*-KO cells occurs beyond initial engraftment. There was a mild but not statistically significant growth defect in the CNS, which could be explained by low penetrance of doxycycline into the CNS[30] (Extended Data Fig. 2j). Lastly, engraftment of mixed KO and control cells directly into the CSF by i.c. injection also demonstrated reduced growth of *SLC31A1*-KO cells compared to control cells, albeit to a lesser degree (Fig. 1f), suggesting that inhibition of cellular copper import impairs leukemic growth in the CSF and not just the cells' ability to migrate to the CNS. Altogether, these findings suggest that inhibiting cellular copper import impairs the growth of ALL both in peripheral organs as well as in the CNS.

https://doi.org/10.1038/s43018-026-01177-4

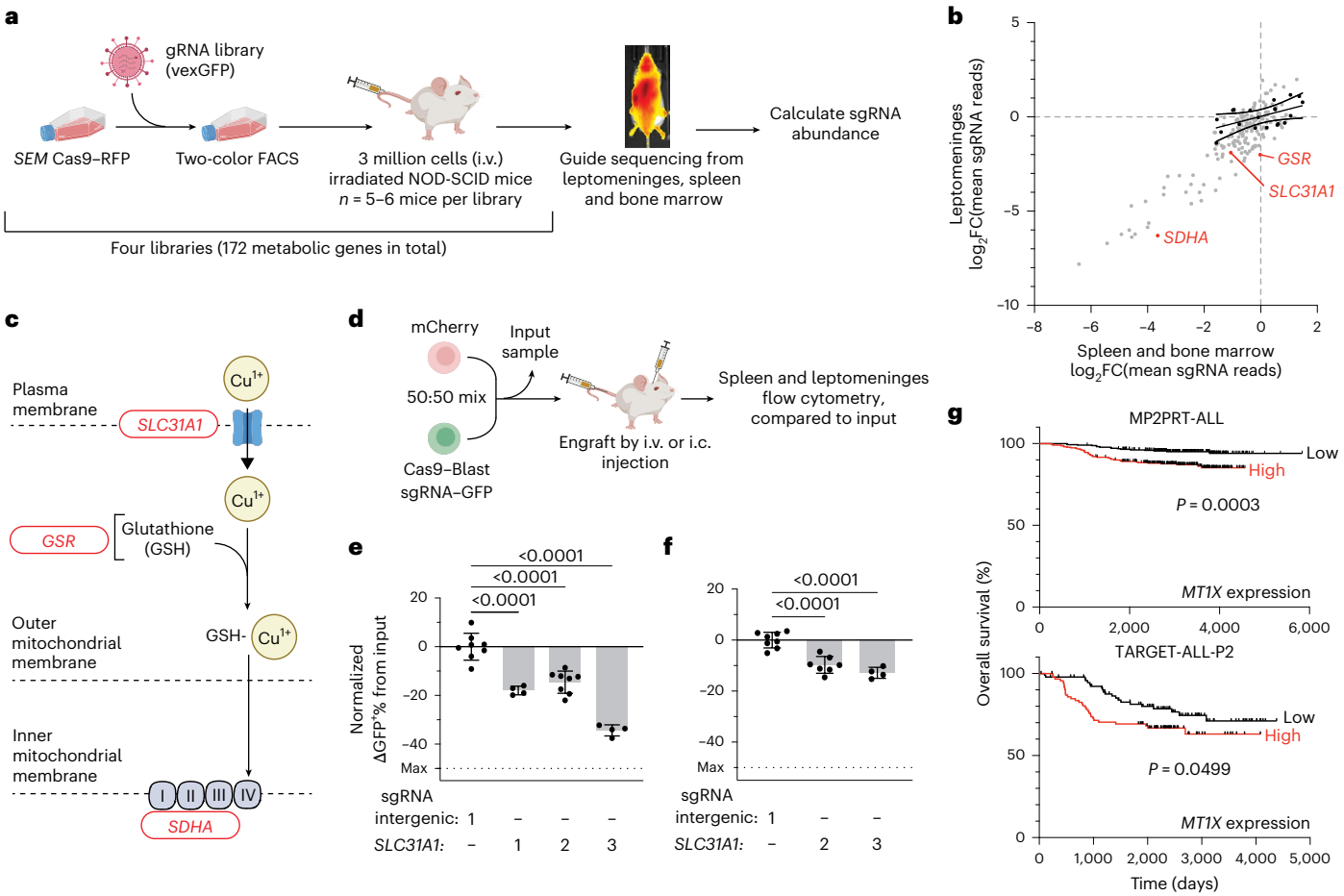

Fig. 1 | Targeted in vivo CRISPR KO screen identifies copper metabolism as an in vivo dependency in ALL. a, Overview of the in vivo CRISPR screen. **b**, CRISPR screen results. Gray dots represent genes in the screen, black dots represent intergenic gRNAs with linear regression and 99% confidence band overlaid ($y = 0.3867x + 0.02825$, $F = 8.3$, DFn = 1, DFd = 18, $P = 0.0099$). Red dots highlight notable genes from the screen. Axes represent the mean $\log_2$ fold change of the MAGeCK-normalized read counts of guides for each gene, relative to the mean read counts of the intergenic guides. **c**, An overview of the linked functions of SLC31A1, GSR and SDHA. **d**, Experimental overview of in vivo competitive mixing experiments to validate single genes from the screen. **e**,**f**, Change in the percentage of GFP^+ cells compared to input, from mice at clinical endpoint that received intergenic or *SLC31A1*-targeting sgRNA cells mixed with control mCherry-expressing cells. Maximal depletion is indicated by a dashed line at −50%. Data are normalized to the mean of the intergenic group and are either from spleens of mice receiving cells by i.v. injection (**e**) or from the leptomeninges of mice receiving cells by intracisternal injection (**f**). Plotted data are the mean ± s.d. *P* values were derived from two-sided Šídák's multiple-comparison tests. For **e**, $n = 8$ intergenic, 4 guide 1, 8 guide 2 and 4 guide 3 mice. For **f**, $n = 8$ intergenic, 7 guide 1 and 4 guide 2 mice. Combined data from two experimental replicates using different guides are presented. Each dot represents an individual mouse. **g**, Kaplan–Meier survival curve of the top and bottom quartiles of participants from the MP2PRT-ALL cohort ($n = 1{,}290$ participants in total) or TARGET-ALL-P2 cohort ($n = 374$ participants in total) with available bone marrow mRNA-sequencing and overall survival data. Vertical dashes represent censored participants. Participants were sorted by *MT1X* expression in TPM and the survival data of the top ('high') and bottom quartiles ('low') were plotted. *P* values were derived from log-rank (Mantel–Cox) tests. Schematics were created in BioRender and further modified in Illustrator; **a**, Wong, A. https://biorender.com/6t8alxv (2026); **c**, Wong, A. https://biorender.com/kbc0x6l (2026); **d**, Wong, A. https://biorender.com/mgcs6yq (2026). FACS, fluorescence-activated cell sorting; FC = fold change; i.v., intravenous; i.c., intracisternal.

Lastly, to assess whether the expression of copper metabolism genes may have prognostic value in persons with ALL, we probed RNA-sequencing data from diagnostic bone marrow samples in the MP2PRT-ALL and TARGET-ALL-P2 trials on the National Institutes of Health (NIH) Genomic Data Commons[31]. Neither *SLC31A1* nor *ATP7A* (a major copper exporter in lymphocytes)[32] mRNA levels were responsive to copper availability in cultured SEM cells (Extended Data Fig. 3a)[33–37] and only *ATP7A* had prognostic value as a single gene (Extended Data Fig. 3b–g). Individual genes within the WikiPathways 'copper homeostasis' gene set (GSEA M39349) also had widely varied and sometimes opposite predictive values across the two datasets (Extended Data Fig. 3h,i). A notable exception was the metallothionein genes, and in particular metallothionein 1X (*MT1X*). High expression of *MT1X* correlated with worse survival in both the MP2PRT-ALL and TARGET-ALL-P2 datasets (Fig. 1g and Extended Data Fig. 3h,i). *MT1X* mRNA transcript levels correlate with copper availability in *SEM* cells (Extended Data Fig. 3j), in agreement with published reports in other cell lines[38–40], suggesting that *MT1X* mRNA may directly reflect the availability of copper in cells. We then assessed whether copper-related gene signatures could have prognostic value by using multiple copper-associated genes. The copper homeostasis gene set (GSEA M39349) again had inconsistent predictive value when considered as a whole (Extended Data Fig. 3k). Instead, we sought to create a copper-related gene signature by mining a published dataset to identify genes that are significantly upregulated vs. downregulated by exposure to copper in vitro[40]. High expression of copper-induced genes and low expression of copper-suppressed genes had consistent and significant prognostic value and correlated with worse survival across both the MP2PRT-ALL and TARGET-ALL-P2 datasets (Extended Data Fig. 3k). As *MT1X* expression could be induced

https://doi.org/10.1038/s43018-026-01177-4

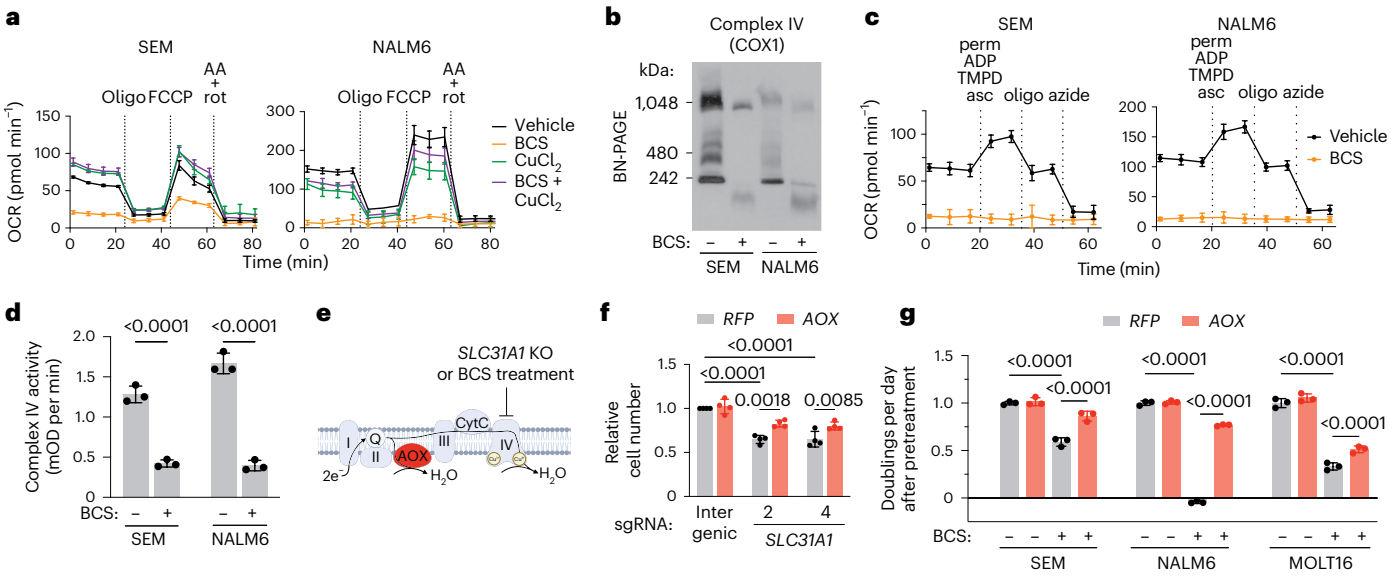

Fig. 2 | Copper depletion inhibits leukemic proliferation through inhibition of the ETC. a, Seahorse MitoStress test on SEM cells (left) or NALM6 cells (right) treated with BCS with or without $CuCl_2$ ($n = 4$ biological replicates/wells for each condition plotted per time point). **b**, BN-PAGE followed by western blot detection of COX1 in native complex IV in SEM cells or NALM6 cells treated with vehicle or BCS. Representative data of two biological replicates are shown, with an additional replicate in the Source Data. **c**, Seahorse assay to measure oxygen consumption rate (OCR) in permeabilized SEM or NALM6 cells following treatment with complex IV substrates ($n = 4$ biological replicates/wells for each condition plotted per time point). **d**, Complex IV enzymatic activity (Abcam) in BCS-treated SEM or NALM6 measured colorimetrically by monitoring the oxidation of reduced cytochrome C over time from 5 µg of mitochondrial lysate immunocaptured on microplate wells coated with anti-complex IV antibodies. ($n = 3$ biological replicates per condition, with each dot representing a separate well). *P* values were derived from two-sided Šídák's multiple-comparison tests. **e**, Schematic of AOX rescue of copper depletion by *SLC31A1* KO or BCS treatment. **f**, Relative cell number after 4 days of control or *SLC31A1*-KO SEM cells overexpressing RFP or AOX ($n = 4$ experimental repeats per condition, with each dot representing the mean of three technical replicates). *P* values were derived from two-sided Šídák's multiple-comparison tests. **g**, Doublings per day from days 5 to 11 (SEM and NALM6) or days 2 to 8 (MOLT16) of BCS treatment in the indicated cell lines overexpressing RFP or AOX ($n = 3$ biological replicates per condition). The doubling rate was calculated as a linear regression of growth over two passages. SEM cells were treated with BCS for 8 days and NALM6 cells were treated for 6 days before the indicated mitochondrial or Seahorse assays. BCS and $CuCl_2$ were used at 50 µM. *P* values were derived from two-sided Šídák's multiple-comparison tests. All plotted values represent the mean ± s.d. AA, antimycin A; oligo, oligomycin; rot, rotenone; perm, XF plasma membrane permeabilizer; ADP, adenosine diphosphate; TMPD = *N*,*N*,*N*,*N*-tetramethyl-*p*-phenylenediamine; asc, ascorbate; OD, optical density.

by exposure to other heavy metals, we also looked at *COX17*, the mitochondrial copper chaperone and found that high expression of *COX17* is associated with worse survival in the MP2PRT-ALL but not the TARGET-ALL-P2 dataset (Extended Data Fig. 3l). Altogether, our in vivo screen, genetic perturbations and human survival data analyses suggest that copper is a metabolic dependency of ALL in vivo.

Copper depletion inhibits leukemic proliferation through inhibition of the ETC

Next, we asked what intracellular function of copper is critical to support leukemia cell proliferation. To address this question, we assessed the cellular consequences of copper depletion by either KO of *SLC31A1* or copper chelation using bathocuproinedisulfonic acid (BCS)[41] in four B-ALL (SEM, NALM6 and REH) and T-ALL (MOLT16) cell lines in culture. We assessed three major intracellular functions of copper relevant to oncogenesis: antioxidant defense[42], kinase signaling (ERK1/2)[21] and ETC activity through complex IV assembly[22] (Extended Data Fig. 4a). Copper depletion in culture had minimal effect on the intracellular GSH/GSSG levels and NADP/NADPH levels in all cell lines tested (Extended Data Fig. 4b,c), arguing against decreased capacity for buffering oxidative stress. Given copper's role in facilitating MEK1-mediated phosphorylation of ERK1/2 (ref. 43), we expected that copper depletion should reduce phospho-ERK1/2 levels. However, copper depletion did not yield consistent effects on phospho-ERK1/2 levels across cell lines, with SEM and MOLT16 cells exhibiting increased phospho-ERK1/2 following BCS treatment and NALM6 and REH exhibiting decreased levels (Extended Data Fig. 4d,e). Our data therefore do not rule out a role for copper in antioxidant defense or MAPK signaling to support leukemia cell proliferation in vivo, especially in the nutrient-deprived CNS. However, findings from both published work and the present work suggest that this is not the case. Notably, copper's role in *MEK1/2* and MAPK signaling have only been shown to affect cancer growth in models that are dependent on oncogenic MAPK signaling[43], which does not apply to the four ALL cell lines we used as far as we are aware. Moreover, we observed proliferative defects (Extended Data Fig. 4f) and suppressed oxygen consumption following copper depletion in vitro across all four cell lines tested (Fig. 2a and Extended Data Fig. 4g), pointing toward inhibited respiration as the culprit behind slowed proliferation at least in culture.

Therefore, we turned our attention to complex IV assembly and copper's role in the ETC. Given the respiration defect of copper-depleted cells (Fig. 2a and Extended Data Fig. 4g), we further interrogated the status of the various respiratory complexes in the SEM and NALM6 cell lines. Copper depletion led to specific reductions in complex IV levels, including the monomeric, dimeric and supercomplex assemblies, as determined by blue native PAGE (BN-PAGE) (Fig. 2b). Western blotting for specific complex IV subunits in denaturing and reducing conditions revealed significant depletion of COX2, mild depletion of COX1 and minimal change in COX4 (Extended Data Fig. 5a,b). Functional assessment of complex IV activity using permeabilized-cell Seahorse and a plate-based immunosorbent biochemical assay confirmed significant loss of complex IV activity (Fig. 2c,d). Although levels of complex I, II and III remained either unchanged or increased upon copper depletion (Extended Data Fig. 5c), metabolite profiling demonstrated that copper depletion decreases the NAD/NADH ratio and increases the succinate/fumarate ratio, suggesting that forward

electron flow through complex I and II is ultimately inhibited by copper depletion (Extended Data Fig. 5d–f). Furthermore, permeabilized Seahorse assays showed no change in oxygen consumption following treatment with either complex I or II substrates (Extended Data Fig. 5g), corroborating complex I and II dysfunction resulting from copper depletion. ETC deficiency resulting from copper depletion was rescued by genetic overexpression of *SLC31A1* or treatment with exogenous copper chloride (Fig. 2a and Extended Data Fig. 5h). Thus, we conclude that a major role of copper in ALL cells is to support ETC activity through complex IV activity.

We next asked whether the observed proliferative defect is a result of copper depletion-induced ETC disruption. To address this, we rescued the activity of the ETC in a copper/complex IV-independent manner by overexpression of alternative oxidase (AOX) from *Ciona intestinalis*[44] (Fig. 2e). AOX overexpression partially rescued the proliferative defect induced by *SLC31A1* KO in SEM cells (Fig. 2f) and BCS treatment in SEM, NALM6 and MOLT16 cells without affecting the proliferative rate of control cells (Fig. 2g and Extended Data Fig. 6a–c). Furthermore, AOX overexpression rescued whole-cell NAD/NADH levels and the NAD/NADH ratio (Extended Data Fig. 6d,e). These data indicate that a key function of copper is to support ETC activity to maintain cell proliferation in ALL cells. The incomplete rescue of growth by AOX may be because of the loss of proton motive force from complexes III and IV (leading ultimately to reduced ATP production) or because of the loss of other copper-dependent intracellular processes (as discussed above) that are not rescued by AOX. BCS treatment does not alter mitochondrial mass nor mitochondrial membrane potential, arguing against loss of mitochondria or mitochondrial permeabilization as a cause for cell death (Extended Data Fig. 6f). Furthermore, treatment of AOX-overexpressing cells two different porphyrin superoxide dismutase (SOD) mimetics (MnTE-2-PyP and MnTBAP)[45] did not further rescue proliferative rate (Extended Data Fig. 6g), suggesting that loss of *SOD1* activity because of copper depletion is not a major contributor to the observed growth defect. Lastly, overexpression of yeast NADH dehydrogenase *NDI1* to bypass complex I did not rescue the proliferative rate of BCS-treated cells (Extended Data Fig. 6h,i), likely because *NDI1* depends on ubiquinone pools that cannot be replenished without functional complex IV. Ultimately, we conclude that copper depletion can restrain leukemia growth through inhibition of ETC activity.

Copper depletion slows leukemia proliferation through inhibition of nucleotide synthesis

It seemed unlikely that ATP depletion as a result of ETC inhibition was the sole cause for slowed growth of copper-depleted leukemia cells, because cancer cells can rely on glycolysis to produce a notable portion of ATP and biosynthetic precursors[46]. To better understand the impact of copper depletion on leukemia cell metabolism, we performed targeted metabolite profiling of *SLC31A1*-KO (SEM) and BCS-treated (SEM, NALM6 and MOLT16) cells. Copper depletion significantly increased levels of pyrimidine synthesis intermediates: carbamoyl aspartic acid (CAA) and dihydroorotate (DHO), purine monophosphates (IMP, AMP and GMP) and decreased levels of aspartate and pyrimidine triphosphates (CTP and UTP) (Fig. 3a–f and Extended Data Fig. 7a–f). CAA and DHO were unable to be detected in MOLT16 cells. Levels of other amino acids were not significantly changed by copper depletion (Extended Data Fig. 7g,h). Lastly, low-dose treatment of SEM cells with the complex IV inhibitor ADDA-5 also decreased aspartate levels with similar effects on pyrimidine synthesis inhibition as BCS treatment (Extended Data Fig. 7i,j), suggesting that perturbed nucleotide metabolism following copper depletion is a direct result of loss of complex IV activity.

We reasoned that the observed disruptions of nucleotide metabolism could be a result of three separate effects. First, inhibition of the ETC leads to defective aspartate synthesis and decreased aspartate abundance, which is critical for nucleotide synthesis (Fig. 3g)[47,48]. Second, inhibition of the ETC reduces ATP production, resulting in the accumulation of purine monophosphates[49]. Third, ETC inhibition could lead to inability of complex III to reduce ubiquinone back to ubiquinol (Fig. 3g), thus inhibiting the activity of pyrimidine synthesis enzyme *DHODH*[44]. This results in the observed accumulation of DHO despite no change in *DHODH* protein levels (Extended Data Fig. 7k). Together, these three mechanisms could explain the decreased aspartate levels, increased CAA/DHO levels and broad perturbations in nucleotide levels.

To address whether perturbed nucleotide metabolism following copper depletion is because of ETC dysfunction, we performed metabolite profiling on copper-depleted cells overexpressing AOX. AOX overexpression in the copper-depleted SEM cells was sufficient to restore DHO, aspartate and most nucleotide levels back to normal (except for IMP, as discussed below) (Extended Data Fig. 7l–n). Additionally, isotope tracing with ^{15}N-labeled amide glutamine in BCS-treated cells revealed increased de novo synthesis and total abundance of CAA and DHO (Fig. 3h and Extended Data Fig. 8a) and significantly reduced de novo synthesis of CTP and UTP (Fig. 3i and Extended Data Fig. 8b), highlighting a substantial pyrimidine synthesis defect. We were unable to detect purine synthesis intermediates in these experiments (PRPP, AICAR or GAR); however, we observed proportionally increased levels of $m+2$ IMP and GMP but not AMP. This suggests that loss of aspartate may inhibit AMP synthesis and lead to accumulation of IMP (Extended Data Fig. 8c,d). In line with this, AOX overexpression did not fully restore aspartate nor IMP levels in BCS-treated cells despite fully rescuing the NAD/NADH ratio (Extended Data Figs. 6e and 7j–l). Analysis of the monophosphate and diphosphate pyrimidines (UMP, UDP and CDP) and purine triphosphates (ATP and GTP) also revealed reduced labeling from ^{15}N-amide glutamine, suggesting a combination of synthesis and phosphorylation defects (Extended Data Fig. 8e–h). Notably, we observed increased DHO synthesis concurrently with decreased aspartate abundance, suggesting that ETC inhibition both increased aspartate consumption through conversion into DHO and reduced aspartate production. Lastly, across the three cell lines we tested, we observed increased $m+1$ GTP (a product of purine salvage) and decreased $m+3$ GTP (a product of de novo purine synthesis) following copper depletion (Extended Data Fig. 8e), consistent with reports that purine salvage increases upon ETC inhibition[49,50]. Therefore, we conclude that copper depletion disrupts pyrimidine and purine synthesis and results in perturbations in nucleotide levels.

We also investigated the effects of another copper chelator: ammonium tetrathiomolybdate (TTM) on cellular metabolism. TTM-treated SEM cells exhibit suppressed respiration (Extended Data Fig. 9a,b), increased levels of IMP and GMP and decreased levels of aspartate and pyrimidine triphosphates (Extended Data Fig. 9c). However, this dose of TTM was rapidly toxic to cells within 3 days (Extended Data Fig. 9d), consistent with TTM's distinct, intracellular mechanism of cytotoxicity as compared to BCS, which chelates copper extracellularly[51].

We next asked whether perturbed nucleotide synthesis is the culprit behind the observed slowed proliferation of copper-depleted ALL cells. To address this, we supplemented copper-depleted leukemia cells with pyruvate and uridine to bolster aspartate and pyrimidine synthesis, respectively[44,47,48] (Fig. 3j). Individual supplementation with either pyruvate or uridine partially rescued the growth rate of *SLC31A1*-KO SEM cells, while dual supplementation further rescued the growth rate of BCS-treated SEM, NALM6 and MOLT16 cells (Fig. 3k,l and Extended Data Fig. 9e). Notably, pyruvate and uridine supplementation rescued the proliferation rate of copper-depleted cells to a similar degree as AOX overexpression, suggesting that the key function of the ETC in leukemia cells is to support nucleotide synthesis. Metabolite profiling revealed that dual supplementation with pyruvate and uridine rescued the NAD/NADH ratio and partially restored aspartate and CAA and DHO levels in copper-depleted SEM cells (Extended Data Fig. 9f–h). Additionally, supplementation of

https://doi.org/10.1038/s43018-026-01177-4

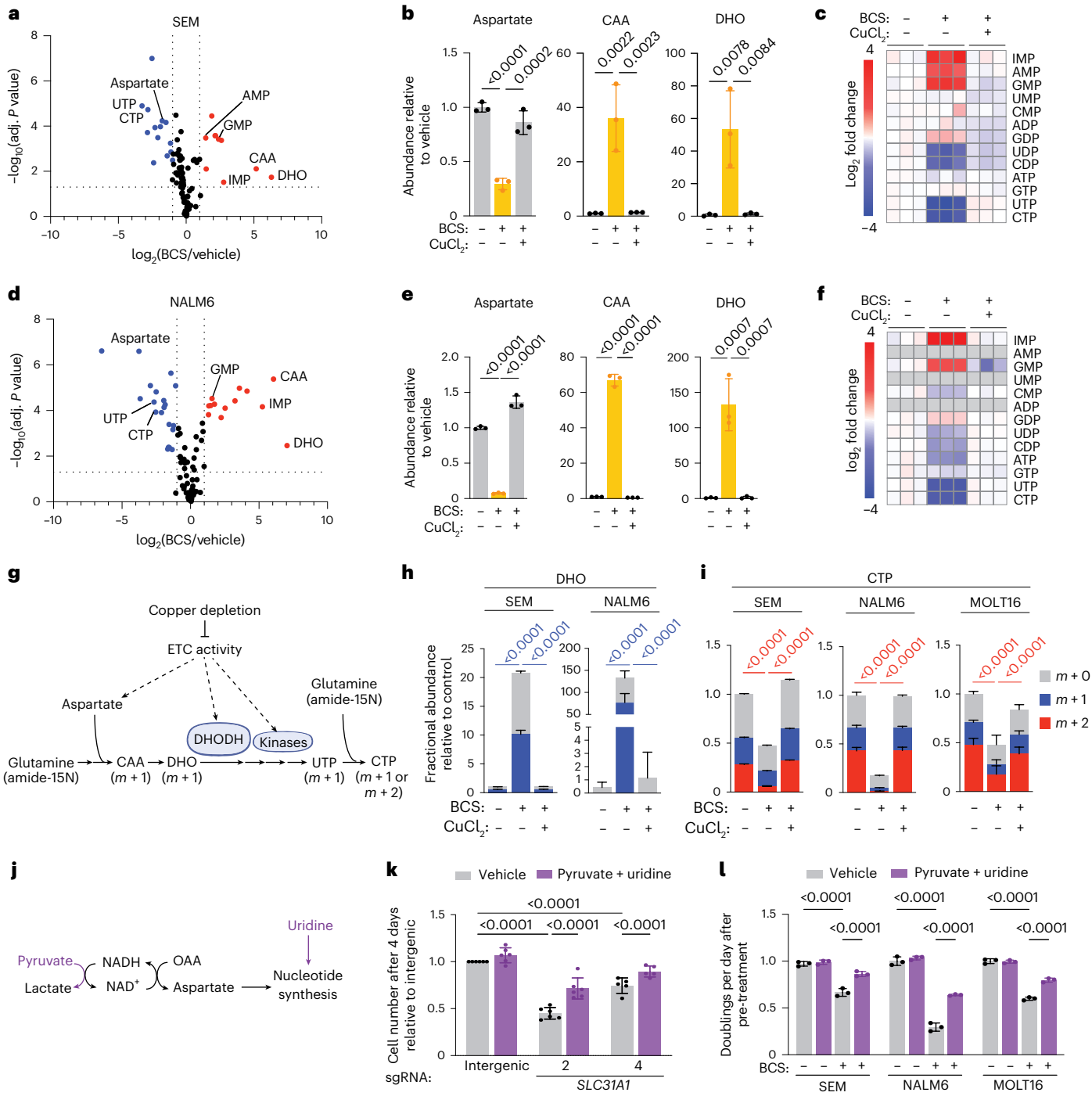

Fig. 3 | Copper depletion slows leukemia cell proliferation through inhibition of nucleotide synthesis. a, Volcano plot of changing metabolites in BCS-treated SEM cells on day 14 ($n = 3$ biological replicates per condition). *P* values were derived from FDR-adjusted two-sided *t*-tests from MetaboAnalyst. **b**, Aspartate, CAA and DHO levels in SEM cells treated with BCS or $CuCl_2$ ($n = 3$ biological replicates per condition). *P* values were derived from two-sided Tukey's multiple-comparison tests. **c**, Nucleotide levels in SEM cells treated with BCS or $CuCl_2$. **d**, Volcano plot depicting metabolite changes between BCS-treated and vehicle-treated NALM6 cells on day 6 ($n = 3$ biological replicates per condition). *P* values were derived from FDR-adjusted two-sided *t*-tests from MetaboAnalyst. **e**, Aspartate, CAA and DHO levels in NALM6 cells treated with BCS or $CuCl_2$ ($n = 3$ biological replicates per condition). *P* values were derived from two-sided Tukey's multiple-comparison tests. **f**, Nucleotide levels in NALM6 cells treated with BCS or $CuCl_2$. **g**, Isotopic labeling scheme of tracing ^{15}N-labeled amide glutamine into pyrimidine synthesis and showing steps that can be inhibited by copper depletion. **h**,**i**, Fractional labeling of metabolites in SEM and NALM6 (**h**) or SEM, NALM6 and MOLT16 (**i**) cells treated with BCS and/or $CuCl_2$ and pulsed for 4 h with ^{15}N-labeled amide glutamine. Labeling is expressed as a fraction of total unlabeled abundances measured in a parallel experiment for DHO (**h**) and CTP (**i**) ($n = 3$ biological replicates per condition). Cells were treated with BCS for 14 days (SEM), 6 days (NALM6) or 8 days (MOLT16). *P* values were derived from two-sided Tukey's multiple-comparison tests. **j**, Scheme showing contribution of pyruvate and uridine to metabolic rescue following copper depletion. **k**, Relative cell number after 4 days of control or *SLC31A1*-KO cells treated with vehicle or combination of pyruvate and uridine ($n = 6$ experimental replicates for intergenic and guide 2, $n = 5$ experimental replicates for guide 4, with each dot representing an experimental replicate as the mean of three technical replicates). **l**, Doublings per day from days 6–10 (SEM cells) or 5–9 (NALM6 and MOLT16 cells) of BCS treatment and either vehicle or pyruvate and uridine ($n = 3$ biological replicates per condition). Plotted data are the mean ± s.d. *P* values were derived from two-sided Šídák's multiple-comparison tests. Cells were treated with uridine (400 µM), pyruvate (1 mM), BCS (50 µM) and $CuCl_2$ (50 µM). OAA, oxaloacetate.

https://doi.org/10.1038/s43018-026-01177-4

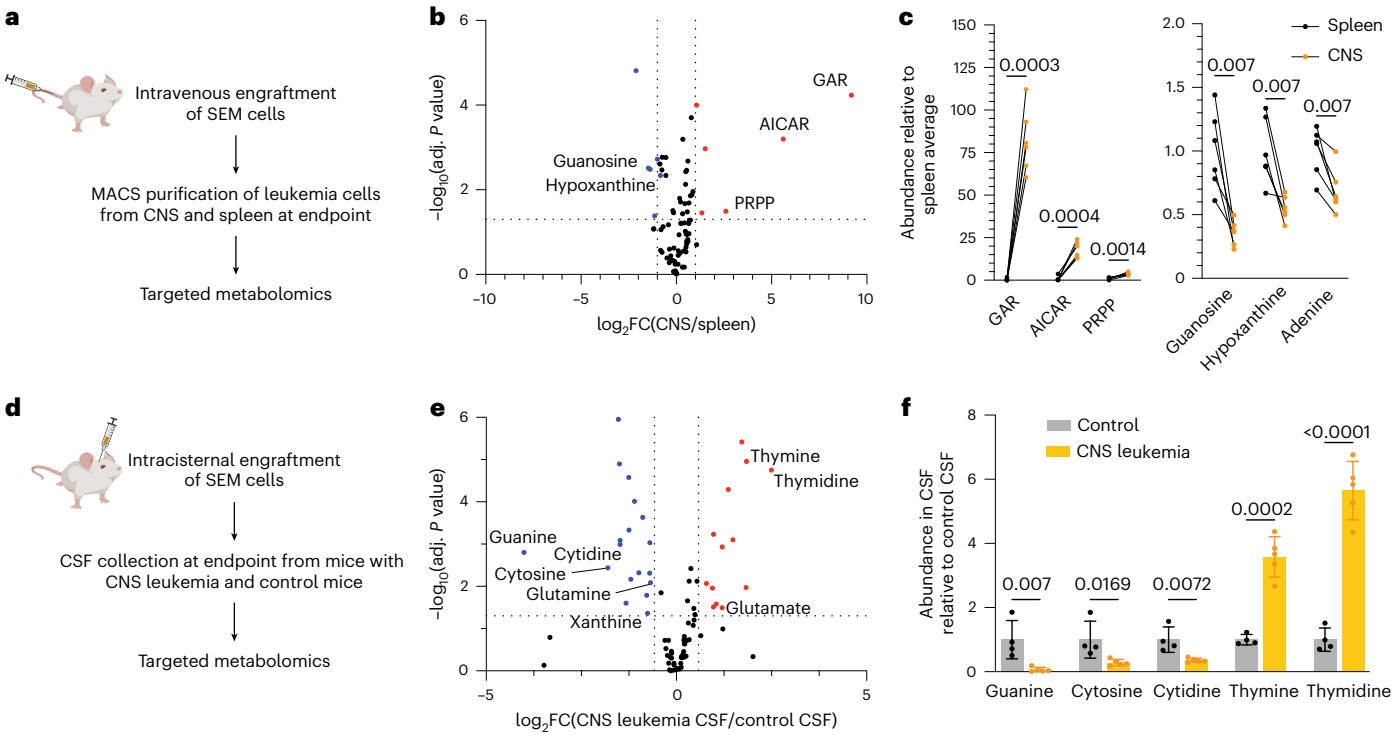

Fig. 4 | Leukemia progression and therapy alter nucleotide precursor levels in mouse CSF. a, Experimental scheme of SEM leukemia cell isolation from the CNS and spleens of mice using MACS. **b**, Volcano plot depicting metabolite changes between CNS and splenic SEM leukemia cells from mice bearing terminal disease ($n = 6$ biological replicates per group). *P* values were derived from FDR-adjusted (two-stage step-up) two-sided *t*-tests from MetaboAnalyst. **c**, Abundance of significantly changing nucleotide synthesis and salvage intermediates or precursors in CNS versus splenic leukemia cells. Plotted values are relative to the mean of the splenic cells ($n = 6$ pairs of CNS and splenic samples from six independent mice, with lines indicating paired samples). *q* values were derived from FDR-corrected paired two-sided *t*-tests. **d**, Experimental scheme of CSF collection from mice with CNS leukemia and control mice. **e**, Volcano plot depicting metabolite changes between CSF from the terminal stage of mice with CNS leukemia compared to control mice ($n = 4$ control CSF samples from individual mice, $n = 5$ CNS leukemia CSF samples from individual mice). *P* values were derived from FDR-adjusted two-sided *t*-tests from MetaboAnalyst. **f**, Abundance of significantly changing nucleotide salvage intermediates or precursors in CSF. Plotted values are relative to control CSF ($n = 4$ control mice, $n = 5$ CNS leukemia mice, with each dot representing a sample from a different mouse). *q* values were derived from FDR-corrected unpaired two-sided t-tests. Error bars indicate the mean ± s.d. *P* values were derived from unpaired two-sided *t*-tests. Schematics were created in BioRender and further modified in Illustrator; **a**, Wong, A. https://biorender.com/tdj07go (2026); **d**, Wong, A. https://biorender.com/tdj07go (2026).

BCS-treated cells with inosine and uridine also partly rescued cell proliferation and DHO levels without changing aspartate levels nor the NAD/NADH ratio (Extended Data Fig. 9i,j). Notably, inosine and uridine supplementation did not rescue to the same extent as AOX (except in MOLT16 cells, in which the trend was reversed), suggesting that at least part of the AOX-driven rescue is dependent on NAD/NADH ratio or ATP production. Overall, these data indicate that nucleotide synthesis is a limiting factor for cell proliferation upon copper depletion.

Leukemia progression and therapy alter levels of nucleotide precursor levels in mouse CSF

As both nucleotide salvage and synthesis have key roles in promoting cancer growth, we investigated the intracellular levels of de novo synthesis intermediates and salvage precursors in CNS versus splenic leukemia cells. First, we developed a method using magnet-activated cell sorting (MACS) to purify SEM cells from the CNS and spleens of mice for metabolite profiling (Fig. 4a). Comparing paired samples from the same mice, we found that SEM cells in the CNS have increased levels of purine synthesis intermediates and decreased levels of salvage precursors (Fig. 4b,c) which may suggest that cells in the CNS exhaust the substrates for nucleotide salvage and increase rates of de novo synthesis. Additionally, metabolite profiling of CSF from mice bearing CNS leukemia and control mice revealed that guanine, cytidine, cytosine, xanthine and glutamine levels were significantly decreased (Fig. 4d–f). Surprisingly, thymine and thymidine levels were increased, suggesting that leukemia cells might selectively scavenge nucleosides within the CSF microenvironment.

Overall, these data could suggest that CNS leukemia cells exhaust salvage precursors and increase de novo synthesis while in the CSF, which might create increased reliance on de novo synthesis that could be targeted therapeutically by copper depletion.

Copper depletion combines with MTX to reduce leukemic growth in vivo

We then asked whether copper depletion can slow ALL progression and combine with existing ALL therapy. Several copper chelators are approved by the US Food and Drug Administration (FDA) and used in the clinic for treatment of Wilson's disease and other syndromes of copper overload[52,53]. Importantly, mild copper depletion is being investigated for prevention of metastasis in high-risk breast cancer cases and is well tolerated by individuals[54]. To achieve copper depletion in our mouse model, we combined zinc acetate (Galzin), an FDA-approved copper-depleting therapy, with a copper-deficient diet (CuD). After 2 weeks, mice on CuD and zinc acetate in the drinking water had significantly lower plasma total copper levels compared to mice on a copper-replete diet (CuR) receiving vehicle (Fig. 5a). To track leukemic progression in mice, we used luciferase-expressing SEM cells and serial bioluminescence imaging (BLI) (Fig. 5b). We found that copper depletion as a monotherapy slows the progression of SEM cell-derived, systemic leukemia (Extended Data Fig. 10a,b). To assess

https://doi.org/10.1038/s43018-026-01177-4

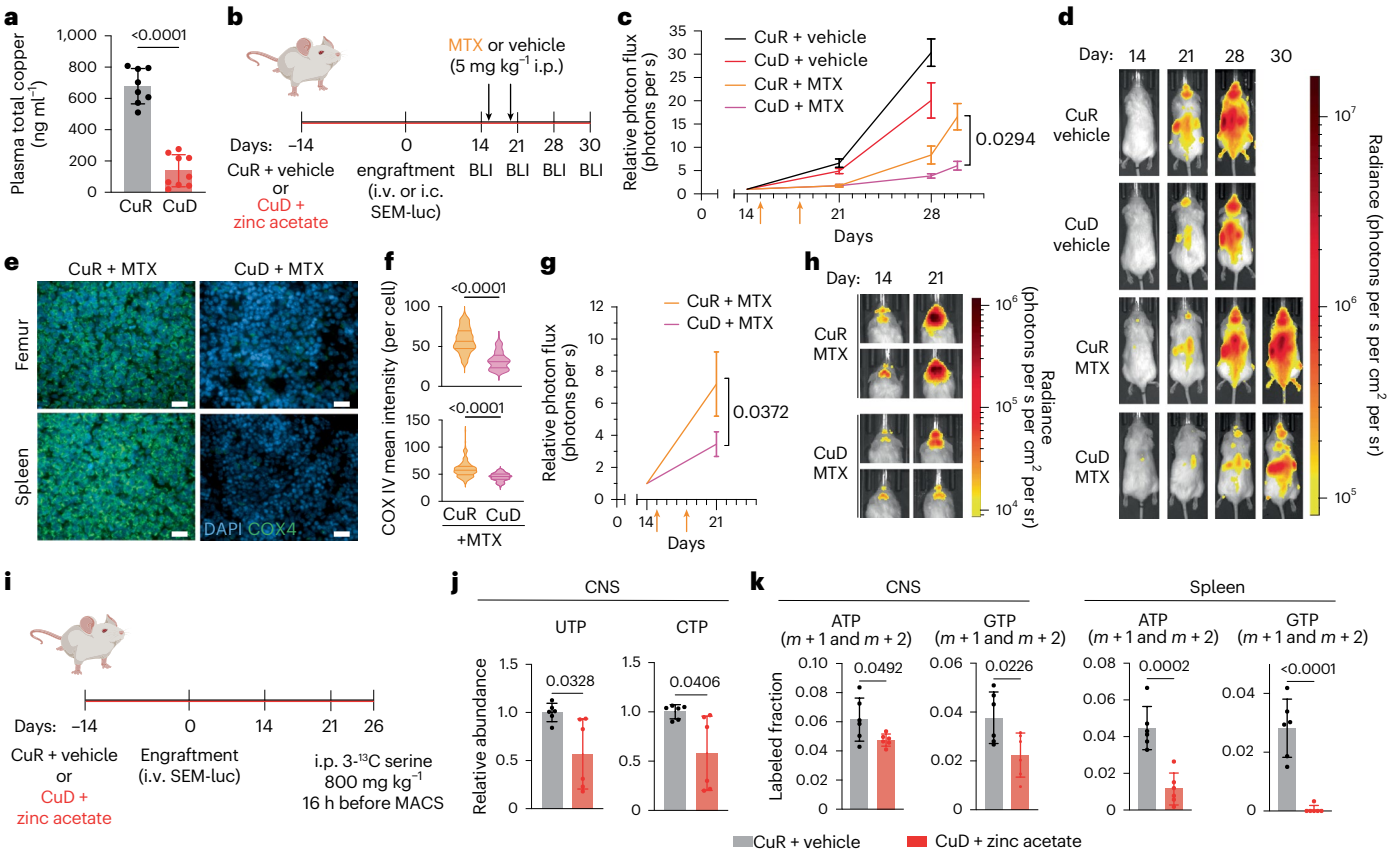

for potential combinatorial effects of CuD with existing antimetabolite therapies used in ALL, we performed targeted metabolite profiling on SEM cells treated with BCS and either 6-mercaptopurine (6-MP) or MTX in culture (Extended Data Fig. 10c). Dual treatment with MTX and BCS further increased AICAR levels, a marker for purine synthesis inhibition (Extended Data Fig. 10d), suggesting an additive effect of copper depletion and MTX. However, copper depletion does not change the half-maximal inhibitory concentration (IC_{50}) of MTX in SEM cells in culture, arguing against a synergistic effect of the two treatments (Extended Data Fig. 10e). These data suggested an additive effect of combining copper depletion with MTX treatment to inhibit ALL growth.

We next assessed whether the combination of MTX and CuD could be used to treat ALL. Copper depletion increased the effect of intraperitoneal (i.p.) MTX on SEM-derived, systemic leukemia in mice (Fig. 5b–d and Extended Data Fig. 10f). Immunofluorescence staining using a human-specific antibody to COX4 demonstrated reduced COX4 levels in the femurs and spleens of CuD + MTX compared to CuR + MTX mice (Fig. 5e,f and Extended Data Fig. 10g–i), confirming a direct effect of copper depletion on ETC integrity in leukemia cells. Additionally, we asked whether copper depletion can be combined with systemic MTX therapy to treat CNS disease. We found that copper depletion enhanced the effect of i.p. MTX in our model of isolated CNS leukemia as measured by serial BLI (Fig. 5g,h). To assess whether nucleotide synthesis is impacted in leukemia cells from copper-depleted mice, we pulsed mice harboring late-stage systemic leukemia with i.p. [3-^{13}C] serine 16 h before purifying the CNS and splenic leukemia cells by MACS (Fig. 5i). Analysis of the unlabeled metabolites revealed decreased levels of UTP and CTP in CNS leukemia cells but not in splenic leukemia cells when comparing CuR and CuD mice (Fig. 5j and Extended Data Fig. 10j), which could be a result of increased reliance on de novo synthesis in the CNS. Critically, levels of $m+1$ and $m+2$ ATP and GTP were significantly decreased in the CNS and splenic leukemia cells of CuD mice (Fig. 5k). Levels of $m+1$ labeled serine were slightly decreased in CNS and splenic cells of CuD mice, which could be a result of increased consumption or reduced uptake of the tracer (Extended Data Fig. 10k). Reduced GSH levels did not change with CuD treatment, arguing against increased oxidative stress as a result of copper depletion (Extended Data Fig. 10l). Lastly, we tested the combined effects of a copper-depleted diet with MTX on two different patient-derived xenograft (PDX) models (CBAB-62871 (B-ALL) and DFAT-25991 (T-ALL)) and found that the combined treatments outperformed MTX alone in inhibiting the progression of disease (Fig. 5l–p, Extended Data Fig. 10m, Supplementary Fig. 1d,e and Supplementary Table 4). Notably, mice on CuD treatments did not exhibit significant weight loss compared to control mice in any of our

Fig. 5 | Dietary copper depletion combines with MTX to reduce leukemic growth in vivo. a, Plasma total copper levels of mice on CuR + vehicle or CuD + zinc acetate treatment for 2 weeks (equivalent to day 0 in scheme in **b**; Methods) as measured by ICP-MS. Plotted values represent the mean ± s.d. Each dot represents an individual mouse ($n = 8$ CuR mice, $n = 9$ CuD mice). Results are the combination of two independent experimental replicates with different mice. *P* values were derived from a Welch's two-sided unpaired *t*-test. **b**, Experimental setup for copper depletion and MTX treatment of leukemic mice (i.p. dosing at days 15 and 18). **c**, Total photon flux from BLI at indicated time points expressed as fold change compared to day 14. Plotted values represent the mean ± s.e.m. ($n = 9$ CuR + vehicle, $n = 8$ CuD + vehicle, $n = 9$ CuR + MTX, $n = 6$ CuD + MTX mice). *P* values were derived from two-sided Tukey's multiple comparisons tests. **d**, Representative BLI images from the indicated days of mice shown in **c**. Each row contains images of the same mouse. **e**, Representative images of femur or spleen sections from CuR + MTX or CuD + MTX mice stained for human COX4 (green) and DAPI (blue). Scale bar, 20 µm. Full quantification of the images is shown in Extended Data Fig. 10g,h. **f**, Violin plots of mean intensity values for COX4 staining per cell for mouse femurs (top) and spleens (bottom). Five cells were quantified per image. For femurs, $n = 205$ and 140 total cells. For spleens, $n = 205$ and 155 cells. Lines indicate quartiles and the median. *P* values were derived from Welch's two-sided unpaired *t*-tests. **g**, Relative photon flux from BLI of mouse heads at indicated days expressed as fold change compared to day 14. Plotted values represent the mean ± s.e.m. ($n = 10$ mice per group). *P* values were derived from two-sided Šídák's multiple-comparison tests. **h**, Representative BLI images from the indicated days in **g**. Each row of BLI images is from the same mouse. **i**, Experimental setup for in vivo [3-^{13}C]serine tracing followed by CNS and splenic SEM leukemia cell isolation by MACS. **j**, Unlabeled abundances of UTP and CTP in CNS SEM leukemia cells. Data are relative to the mean of CuR + vehicle mice ($n = 6$ biological replicates per group). Plotted values represent the mean ± s.d. *P* values were derived from Welch's two-sided unpaired *t*-test. **k**, Sum of $m + 1$ and $m + 2$ ^{13}C-labeled fractions of ATP and GTP in CNS SEM leukemia cells and splenic SEM leukemia cells ($n = 6$ biological replicates per group). Plotted values represent the mean ± s.d. *P* values were derived from Welch's two-sided unpaired *t*-test. **l**, Scheme of experiment to assess effect of CuD or CuR diets with MTX treatment in PDX models of ALL. Mice were placed on experimental diets one day after i.v. engraftment of PDX cells, given i.p. doses of MTX or vehicle at indicated time points and monitored for percentage of human CD45$^+$ cells in peripheral blood (hCD45$^+$%) by cheek bleeding. **m**, Percentage of hCD45$^+$ cells in peripheral blood at indicated time points for the CBAB-62871 PDX model. Plotted values represent the mean ± s.e.m. ($n = 6$ CuR + vehicle mice, $n = 5$ CuD + vehicle mice, $n = 16$ CuR + MTX mice, $n = 17$ CuD + MTX mice from weeks 1 to 6). Combined data from two experimental replicates are shown. In the second replicate, mice were also measured at week 7 ($n = 10$ for CuR + MTX, $n = 11$ for CuD + MTX). *P* values were derived from testing for differences in linear regression slopes between CuR + MTX and CuD + MTX across weeks 1–7 ($F = 15.30$, DFn = 1, DFd = 182, $P = 0.0001$; slope = 6.817 for CuR + MTX versus 2.702 for CuD + MTX). No outliers were removed. **n**, Percentage of hCD45$^+$ cells in peripheral blood at week 7 for CBAB-62871 ($n = 10$ CuR + MTX mice, $n = 11$ CuD + MTX mice, with each point representing an individual mouse). Plotted values represent the mean ± s.d. *P* values were derived from Welch's two-sided unpaired *t*-tests. **o**, Percentage of hCD45$^+$ cells in peripheral blood at indicated time points in the DFAT-25991 PDX model. Plotted values represent the mean ± s.e.m. ($n = 8$ mice from weeks 4 to 6, $n = 5$ mice per group at week 7). *P* values were derived from testing for differences in linear regression slopes between CuR + MTX and CuD + MTX across weeks 4–7 ($F = 11.42$. DFn = 1, DFd = 54, $P = 0.0014$; slope = 31.32 for CuR + MTX versus 15.43 for CuD + MTX. No outliers were removed. **p**, Percentage of hCD45$^+$ cells in peripheral blood at week 7 for DFAT-25991 ($n = 5$ biological replicates (individual mice) per group). Plotted values represent the mean ± s.d. *P* values were derived from Welch's two-sided unpaired *t*-tests. *P* values were derived from testing for differences in the best-fit values for the growth constant *k* in multiple logistic regressions. PDX cells were obtained from ProXE as a gift from J. Perry in K. Stegmaier's lab. Schematics created in BioRender and further modified in Illustrator; **i**, Wong, A. https://biorender.com/q3p83gn (2026); **l**, Wong, A. https://biorender.com/q3p83gn (2026).

experiments (Extended Data Fig. 10n–r). Overall, these data provide a proof of concept that copper depletion represents an actionable, nutritional handle to perturb ETC activity and potentiate leukemia therapy for systemic disease and in the hard-to-treat CNS.

Discussion

Our data suggest that copper metabolism is an actionable nutrient dependency for ALL. Using in vivo functional genomics, we elucidated copper metabolism as a dependency of ALL cells both systemically and in the CNS. Mechanistically, we found that depletion of the micronutrient copper slows leukemia cell proliferation through inhibition of ETC activity and disruption of nucleotide synthesis. Systemic depletion of copper enhances the effect of the drug MTX, which is standard of care for ALL. This combinatorial approach inhibits ALL growth in both cell-line-derived and PDX ALL models in vivo. This may suggest an additive benefit of copper depletion concurrent with existing therapy in the clinical setting. Lastly, our data highlight a combinatorial effect of copper depletion and MTX on slowing the growth of leukemia cells within the CSF, suggesting that a nutritional perturbation could potentiate therapy for CNS leukemia.

Beyond therapeutic applications, this work also raises the possibility that circulating copper levels could be predictive of overall outcome and potential emergence of drug-resistant disease. In small-scale studies, circulating copper levels were reported to be increased in patients with ALL[55]; however, most circulating copper is bound to the acute-phase reactant ceruloplasmin. Circulating ceruloplasmin levels increase in response to broad proinflammatory stimuli[56], which raises the possibility of a connection between inflammation and copper availability to leukemic blasts. It is, therefore, possible that the degree of systemic inflammation and circulating copper in persons with ALL could be a contributor to or predictor of survival or response to therapy. Additional studies tracking the longitudinal and cohort levels of circulating copper would be needed to establish such correlations.

Systemic copper depletion is the manifestation of Menkes disease. Importantly, decades of experience and research into Menkes disease have highlighted that profound copper depletion leads to abnormal neurodevelopment, resulting in developmental regression and seizures in childhood[57]. Open questions, therefore, include whether the degree of copper depletion needed for anticancer effect will result in appreciable neurotoxicities in treated individuals. This is complicated by the different developmental stages of persons who present with ALL and the prolonged duration of ALL therapy regimens that can span months and even years. In recent clinical trials testing the efficacy of the copper chelator TTM in preventing breast cancer metastasis, participants were copper-depleted to 20–50% of normal levels (as measured by serum ceruloplasmin), which was well tolerated, with <5% of participants experiencing toxicity presenting as neutropenia or leukopenia[54]. The median age in this trial was 29 years; thus, the safety concerns of potentially applying copper chelation in infants or children with ALL must be considered.

In terms of our advancement of the understanding of copper biology, this study highlights the central and essential role of copper in supporting nucleotide metabolism and the ETC in rapidly dividing cancer cells. However, it is possible that copper has other essential roles in various cellular functions in ALL in vivo and these might be revealed by further investigation of copper function in vivo. For example, application of the AOX rescue in an in vivo context would help to further solidify the essentiality of copper's role in supporting ETC activity in leukemia. Furthermore, rescue experiments in this study that bolstered either nucleotide metabolism or ETC function were unable to fully rescue the proliferative defects of copper-depleted cells. This incomplete rescue could be attributed to metalloallosteric roles of copper (such as in autophagy[58], endoplasmic reticulum stress[59] or kinase signaling[43,60]) in leukemia cells. Additional studies are needed to characterize these additional functions of copper in driving cell proliferation and determine whether copper depletion may lead to redistribution of copper

or rewiring of intracellular metabolism and signaling networks that ultimately slow the proliferation of leukemia cells.

Overall, our work highlights a new potential therapeutic avenue for CNS leukemia. Using a genetic screen, we uncovered copper metabolism and oxidative phosphorylation as in vivo dependencies in ALL and propose copper depletion as a novel therapeutic strategy for systemic and CNS ALL.

Methods

This study followed all relevant ethical regulations and was approved by the Boston Children's Hospital Institutional Biosafety Committee, Institutional Review Board and Institutional Animal Care and Use Committee (IACUC).

Cell lines and cell culture

Cell lines were obtained from the following sources: SEM and NALM6, D. M. Sabatini (Massachusetts Institute of Technology); MOLT4, MOLT16, PF382 and REH, A. Gutierrez (Dana-Farber Cancer Institute, validated by short tandem repeat profiling at the Dana-Farber Cancer Institute Molecular Diagnostics Core in December 2022). All cells were cultured in RPMI-1640 + 10% FBS + 1× penicillin–streptomycin at 37 °C with 5% CO_2 and tested monthly for *Mycoplasma*. Catalog numbers and doses are provided in Supplementary Table 5. MnTBAP stocks were prepared in 0.1 M NaOH; other stock solutions were prepared in PBS or DMSO (ADDA-5, TTM, trametinib and drugs for Seahorse assays).

For cell-doubling experiments, cells were seeded at 250,000 cells per ml for 2–3 days, then counted using hemocytometers and reseeded (125,000 or 250,000 every 2 or 3 days). Cell doublings were calculated as follows:

$$\text{Cell doublings}_{\text{day 2}} = \log_2(\text{density}_{\text{day 2}}/\text{density}_{\text{day 0}})$$

Doubling rate was calculated as a linear regression of at least three cell counts across 5–6 days. For cell growth experiments across 4 days, cells were seeded at 100,000 cells per ml.

IC_{50} dose–response curves

Cells were seeded at a cell density of 100,000 cells per ml in 96-well plates with treatments in pentaplicate. After 4 days, the CellTiter-Glo cell viability assay kit was used. Dose–response curves and IC_{50} values were determined by best-fit analyses using GraphPad Prism.

Immunoblot and immunoprecipitation

Cells were lysed in RIPA buffer with protease inhibitors, quantified using bicinchoninic acid (BCA) assay and prepared in 5× sample buffer. Samples were not boiled when analyzing mitochondrial proteins. Then, 20 µg of protein lysate was used for SDS–PAGE and transferred onto 0.45 µM PVDF. Blots were blocked using 5% milk in Tris-buffered saline with Tween-20 (TBST) for 1 h at room temperature, washed three times with TBST and then incubated in primary antibody at 4 °C overnight. A list of antibodies used is provided in the Nature Portfolio Reporting Summary.

For SLC31A1 immunoblotting from cell lysates, immunoprecipitation was performed using protein A/G magnetic beads without crosslinking. Buffer composition and preparation protocols are listed in Supplementary Table 5. Next, 25 µl of beads per sample were washed three times with 500 µl of coupling buffer using a magnetic stand. Then, 100 µl of coupling buffer and 10 µl of primary antibody were added per sample and beads were placed on an inversion mixer for 1 h at room temperature. Beads were then washed twice with 500 µl of coupling buffer, twice with 500 µl of MCLB and stored on ice for up to 24 h. A total of 5 million cells were washed with PBS and then resuspended in 250 µL MCLB (with 1 mM DTT and Roche protease inhibitor cocktail). Lysed cells were placed on an inverting mixer for 20 min at 4 °C and then spun at 16,100 rcf for 10 min and 50 µl of the supernatant was quantified with BCA assay and used as 'input' samples for immunoblotting.

Next, 200 µl of supernatant was mixed with antibody-bound beads and incubated on an inverting mixer overnight at 4 °C. Samples were washed twice with 500 µl with wash buffer, once with water and then eluted in 100 µl of elution buffer for 10 min at room temperature on an inverting mixer. Finally, 15 µl of neutralization buffer was added to the eluent.

BN-PAGE and complex IV enzymatic activity assays

Crude mitochondrial isolates were produced as described previously[61] and quantified by BCA assay. Complex IV enzyme activity was measured according to the manufacturer's instructions for 70 min of data collection. BN-PAGE was conducted as described previously[61].

Flow cytometry

Flow cytometry was performed on a BD Fortessa or BD FACSMelody operating BD FACSDIVA (version 8.0.1) or FACS Chorus (version 3.0) as described previously[62]. Cells were washed with FACS buffer, stained with primary antibodies for 30 min, washed and analyzed. For indirect staining of SLC31A1, cells were washed, incubated for 30 min with the primary antibody, washed and then incubated for 30 min with secondary antibody. For cell sorting, all steps were performed at room temperature to preserve viability. A list of antibodies is provided in the Nature Portfolio Reporting Summary.

Mitochondrial membrane potential and mitochondrial mass measurement

Cells were seeded at 1 million cells per ml in medium containing 500 nM TMRM and 2.5 µM MitoSpy green FM at 37 °C in an incubator for 30 min. Cells were then washed once in FACS buffer and analyzed by flow cytometry.

Gene expression by qPCR

RNA was extracted from cell pellets using RNAzol. First, 1 µg of RNA per sample was reverse-transcribed the LunaScript RT supermix. Analysis using SYBR green was performed on a QuantStudio 7 Pro (Applied Biosystems) qPCR instrument. The reference genes for all qPCR reactions were β-actin and UBC. qPCR primers can be found in Supplementary Table 5.

Seahorse analysis

The Seahorse plate was treated with 1× poly(L-lysine) solution in water for 15 min and then washed three times with 1× PBS. Cells were washed once in prewarmed Seahorse RPMI and 100,000 cells were plated per well in pentaplicates. Cells were centrifuged at 350*g* for 1 min with no braking and then incubated at 37 °C for 1 h in an incubator without CO_2. The mitochondrial stress test was performed with 1 µM carbonyl cyanide-*p*-trifluoromethoxyphenylhydrazone (FCCP), 2 µM oligomycin, 500 nM rotenone and 500 nM antimycin A. Analysis was performed using Wave software (Agilent Technologies).

Permeabilized-cell Seahorse assays were performed as previously described[63].

Metabolite profiling by mass spectrometry (MS)

Polar metabolite detection. A total of 1.5 million cells from culture were collected by centrifugation, washed with 0.9% liquid chromatography (LC)–MS NaCl and resuspended in 400 µl of ice-cold 100% LC–MS methanol and 100 µl of LC–MS water with additives as described previously[64]. For CSF metabolomics, 10 µl of mouse CSF was extracted in 160 µl of methanol with standards + 40 µl of water with additives as above. Ellman's reagent solution was prepared fresh on the day of the experiment.

Details of sample preparation, chromatographic separation and analysis per experiment can be found on Metabolomics Workbench (https://doi.org/10.21228/M8Q250).

Analysis for 5-methyl tetrahydrofolate was performed as previously described[62].

Metabolomics data analysis. Polar metabolites were relatively quantified while referencing an in-house library of chemical standards and using TraceFinder 4.1 (Thermo Fisher Scientific), with a 5-ppm mass tolerance as previously described[62]. Normalization was performed in R using scripts found on GitHub (www.github.com/FrozenGas/KanarekLabTraceFinderRScripts). The TraceFinder library used for analysis can be found in Supplementary Table 6.

Nucleotide heat maps were generated using Morpheus (https://software.broadinstitute.org/morpheus) and further edited in Adobe Illustrator.

Gene targeting using sgRNAs

sgRNAs (from the Broad Institute CRISPick tool[65,66]; sequences in Supplementary Table 5) were cloned into the doxycycline-inducible sgRNA vector FgH1tUTG (Addgene, 70183). Guides with 5′-TCCCG-3′ overhang on the forward sequence and 5′-AAAC-3′ overhangs on the reverse sequence were annealed and phosphorylated using T4 polynucleotide kinase and ligated into the vector in one step using BsmBI-v2 and T4 ligase. The subsequent vector was transformed into chemically competent DH5a cells for plasmid propagation.

CRISPR-resistant SLC31A1 cloning

A CRISPR-resistant *SLC31A1* coding sequence with a 3′ 3× G4S linker and HA tag and 5′ BamHI and 3′ MluI restriction enzyme sites was ordered as a gene block. Following PCR amplification, the product was digested using BamHI and MluI and purified using the Monarch PCR and DNA cleanup kit. The pLEX_TRC202 and pLEX_TRC203 plasmids were also digested, linearized plasmids were gel-purified and the *SLC31A1* open reading frame was ligated in using T4 ligase.

Plasmids used in this study

FUW-RLuc-T2A-PuroR (Addgene, 102320), FgH1tUTG (Addgene, 70183), ΔVPR envelope (Addgene, 8455), CMV VSV-G (Addgene, 8454), Cas9–RFP lentiviral particles (Sigma-Aldrich, Cas9-RFPV-200uL), Cas9-Blast (Addgene, 52962), pAW13.lentiguide.mCherry (Addgene, 104375) and pLEX_TRC202 and pLEX_TRC203 (D.M. Sabatini).

pLV-RFP, pLV-AOX-IRES-RFP and pLV-NDI1-IRES-RFP were obtained as gifts from N. Chandel's lab.

Lentivirus production

HEK-293T cells were transfected with 5 µg of transfer plasmid, 4 µg of ΔVPR envelope (Addgene, 8455) and 1 µg of CMV VSV-G (Addgene, 8454) diluted in either jetPRIME transfection reagent or TransIT-VirusGEN transfection reagent. The next day, the medium was replaced with 8 ml of DMEM + 30%FBS. After 48 h, virus-containing supernatants were collected and filtered through a 0.45-µm syringe filter.

Lentiviral transduction of cell lines

Cells were seeded at 2,500,000 cells per ml in six-well plates in 2 ml of culture medium containing 1:1,000 polybrene and centrifuged at 931*g* for 105 min at 30 °C. After spinning, 2 ml of complete medium was added to each well. The next day, cells were reseeded into fresh culture medium. After 48–72 h, cells were selected using 1 µg ml^{-1} puromycin, 10 µg ml^{-1} blasticidin or by cell sorting. For *SLC31A1* inducible KO cells, doxycycline (2 µg ml^{-1}) was added for 72 h and >500,000 *SLC31A1*-negative cells were sorted using indirect staining. For intergenic sgRNAs, *SLC31A1*-positive cells were sorted.

^{15}N-labeled amide glutamine tracing

Glutamine-free RPMI was supplemented with 10% dialyzed FBS, 1× penicillin–streptomycin and unlabeled glutamine or ^{15}N-labeled amide glutamine. Total glutamine concentration in all conditions was 300 mg L^{-1}. Following 4 h of culture in labeled or unlabeled conditions, cells were washed and prepared for LC–MS profiling as described above. During analysis, the mass of the extra neutron (m = 0.997) was added to the expected m/z, enabling calculation of the percentage labeling for each nitrogen (m + 1, m + 2, m + 3, etc.) with correction for the natural abundance (IsoCorrectoR)[67].

Inductively coupled plasma (ICP)-MS analysis of copper

Copper levels were quantified using ICP-MS. Whole mouse blood was collected by submandibular bleeding into a heparinized tube (VWR, 103093-113) and then spun at 2,000*g* for 10 min at 4 °C. Next, 10 µl of the supernatant plasma was transferred to a nitric-acid-washed 1.5-ml tube and frozen at −80 °C until digestion and analysis. Sample digestion and ICP-MS analysis were conducted by the Biomolecular MS Core within the Center of Excellence in Environmental Toxicology at the University of Pennsylvania. All samples were spiked with internal standards: yttrium-89 at 1 ppb and terbium-159 at 0.2 ppb final concentrations. Digestion was performed by adding 250 µl of concentrated HNO_3 to each sample, followed by incubation at 60 °C for 48 h. Digested samples were then diluted to a final volume of 5 ml using metal-free Milli-Q water.

A calibration curve was prepared concurrently using a premixed metal ion standard, starting at 250 ppb and serially diluted twofold to 0.12 ppb. Copper levels were measured using an iCAP RQ ICP-MS instrument (Thermo Fisher Scientific).

Participant survival curves

Participant survival and transcripts per million (TPM) for *MT1X*, *SLC31A1* and *ATP7A* from the Therapeutically Applicable Research to Generate Effective Treatments (TARGET) initiative and Molecular Profiling to Predict Response to Treatment in ALL (MP2PRT-ALL) cohorts were downloaded from the GDC and Xena on October 1, 2025[68]. For participants with multiple samples, only the first diagnostic bone marrow sample was used. Both B and T cell ALL cases from TARGET-ALL-P2 were included. Overall survival was plotted for the upper and lower quartiles and *P* value testing was conducted using GraphPad Prism version 10. For analyses using gene sets, the 'gene set contrast' function in SurvivalGenie 2.0 (https://bhasinlab.bmi.emory.edu/SurvivalGenie2/coexp-module/input) was used[69].

Animal work

Animal work was approved by the BCH IACUC under protocol 2068. Mice were deemed terminally ill and euthanized if they exhibited symptoms of lethargy, a drop in weight (10% over a day or 20% since the beginning of the experiment), reduced appetite, a lack of movement, a hunched back or hair loss. These criteria were not exceeded in our experiments. All mice used were mixed-sex NOD.CB17-*Prkdc*^{scid}/NCrCrl (originally purchased from Charles River and maintained at the BCH ARCH animal facility by self-breeding) and 5–12 weeks of age at the start of each experiment. Unless otherwise specified, mice were cohoused in a temperature-controlled and humidity-controlled room (21 ± 1.5 °C, 35–70% humidity) in autoclaved OptiMice cages on 12-h light–dark cycles (7 a.m.–7 p.m.) and received autoclaved water and a Prolab RMH 3500 Autoclavable diet ad libitum.

Cell injections (i.v. and i.c.)

To prepare cells for injection, cells were washed once with PBS and then resuspended in 0.9% NaCl at the indicated concentrations below.

For i.v. injections, 3 million cells per 200 µl were prepared in sterile 0.9% NaCl. The 27G insulin syringes were flushed using an extra aliquot of cells and then loaded with 200 µl of cells. Irradiated mice (250 rads within 4 h of injection) were restrained using a mouse tail illuminator and restrainer (Braintree Scientific) and cells were injected into the tail vein.

For i.c. injections, mice were anesthetized using isoflurane (3–5% in pure oxygen) and transferred onto a surgical chuck with a low-profile nose cone and facemask. Mice were draped with the neck in 90° flexion across a 15-ml centrifuge tube and the space between the ears was shaved and prepared using betadine and 70% ethanol. A 30G insulin syringe was marked at 3.5 mm using lab tape and flushed with a cell mixture (50,000 cells per 10 µl) before 10 µl of the cell mixture was drawn up. The needle was inserted midline between the posterior skull and C1 vertebrae approximately 3.5 mm deep. After slowly injecting with a 10-s pause at the end, the site was wiped with 70% ethanol. Mice were monitored and euthanized if paralysis, abnormal gait or head tilt was observed following recovery.

Mouse CSF collection

Mouse CSF collection was performed as described previously[11] with mice anesthetized using ketamine and xylazine (100–120 mg kg^{-1} and 10 mg kg^{-1} by i.p. injection).

In vivo barcoding experiment

SEM cells were transduced with a lentiviral library (derived from the pRDA_206 backbone from the Broad Institute) encoding ~25,700 genetic barcodes (gift from M. Schwartz) at a multiplicity of infection (MOI) of 0.3–0.4. A total of ~15 million vexGFP$^+$ cells were sorted to maintain >500× coverage of all barcodes and then engrafted by i.v. injection into irradiated NOD-SCID mice. At the endpoint, cells were collected by blunt dissection from the skull and spleen and filtered through a 70-µm cell strainer using a 3-ml syringe plunger. For bone marrow samples, femurs and tibiae from mice were placed in a petri dish with PBS and flushed using a 25G needle and 3-ml syringe. To collect cells from the peripheral blood, 500–600 µl of blood was collected in an EDTA-flushed 1-ml syringe by cardiac. All samples were subjected to RBC lysis for 10 min, washed once with PBS, pelleted and frozen at −80 °C until further processing.

Genomic DNA was extracted using the QIAamp DNA mini kit and submitted for NGS. As a proxy for the number of barcodes retained within each site, we ranked the barcodes by most to least number of reads and calculated the number of barcodes whose cumulative sum added up to 90% of total reads from each site.

In vivo CRISPR screens

Each library contained 172 sgRNAs targeting 43 library-unique genes, with four sgRNAs per gene and 20 shared, control sgRNAs targeting noncoding intergenic loci (Extended Data Fig. 1e). Plasmid pools were obtained from the Broad Institute (clone pools 1726–1729). For each screen, lentiviral production was performed in-house in triplicate in 15-cm plates with 293T cells at 60–70% confluency using TransIT-VirusGEN transfection reagent (MIR6703). In total, 8 µg of ΔVPR, 2 µg of VSV-G and 10 µg of pool plasmid was used per transfection. SEM cells were transduced at 0.3–0.4 MOI (determined by vexGFP positivity following transduction). Then, 48 h after lentiviral transduction, 22 million vexGFP$^+$ cells were sorted in batches over the course of a day. The next day, mice were engrafted with 3 million cells each by tail-vein injection. Aliquots of cells at injection were frozen down as reference samples. A total of 5–6 mice were used per library and the screens were staggered, with all mice for one library engrafted at the same time. At the humane endpoint, cells were collected from the skull, spleen, bone marrow and peripheral blood as described above and genomic DNA was extracted for NGS.

sgRNA reads were processed using MAGeCK[19], using paired analysis comparing the brain to the sum of reads from the spleen and bone marrow and normalizing to the median of control intergenic sgRNAs. Each mouse was considered its own replicate for each library. For scatter plots, the mean sgRNA reads for each gene were taken from the MAGeCK output files.

Mouse drug treatments and in vivo imaging system (IVIS)

A 1 mg ml^{-1} stock of MTX was prepared in sterile PBS and mice were given 5 mg kg^{-1} doses i.p. in 200 µl. BLI was performed using the IVIS Spectrum (PerkinElmer) operating the LivingImage (version 4.8.2) software. Mice were given i.p. injection of 50 µg of water-soluble substrate coelenterazine dissolved in 100 µl of 0.9% sterile NaCl. After 10 min, mice were anesthetized with isoflurane (3–4% in oxygen) and then imaged. For in vivo doxycycline induction, doxycycline was supplemented at 0.4 mg ml^{-1} with 2% sucrose in drinking water.

Copper depletion in vivo

Mice 5 weeks or older were randomized to a CuR (6 ppm; Teklad TD.240097) or CuD (0.3–0.7 ppm; Teklad TD.240098) diet. If applicable, drinking water contained 2% sucrose with or without 2 g L^{-1} zinc acetate for 4 weeks (2 weeks before engraftment and 2 weeks after); after this treatment period, all mice were switched to autoclaved water. Mice were allowed to consume food and water ad libitum and food and water were replaced weekly.

PDX models of ALL

PDX cells (CBAB-62871 and DFAT-25991) were obtained from the Public Repository of Xenografts (ProXE)[70] as a gift from J. Perry and K. Stegmaier. All PDX cells used were under the fifth passage. Irradiated mice were engrafted by i.v. injection with 1 million PDX cells. The next day, mice were randomized to treatments. To monitor the progression of the disease, 2–3 drops of blood were collected by submandibular bleeding into a heparinized tube and lysed for 5 min using 1 ml of ACK lysis buffer or red blood cell (RBC) lysis buffer. Samples were washed in FACS buffer and stained in 250 µl of FACS buffer (antibodies listed in Nature Portfolio Reporting Summary) in a 96-well U-bottom plate for 30 min at 4 °C in the dark.

Data on PDXs used in this study are available in Supplementary Table 4.

MACS of human leukemia cells from mice

Mice were anesthetized with ketamine and xylazine (100–120 mg kg^{-1}, 10 mg kg^{-1} by i.p. injection) and leukemia cells were isolated from the skulls and spleens as described above. Cells were resuspended in 160 µl of FACS buffer; 40 µl of mouse cell depletion cocktail was added and then incubated on ice for 5 min before column sorting using an LS column and a QuadroMACS magnet per manufacturer instructions. The flowthrough was spun at 4,000*g* for 1 min at 4 °C, washed in 1 ml of 0.9% LC–MS-grade NaCl, spun for 20 s at 4 °C at 21,000 rcf and then used for polar metabolite detection as described above.

For in vivo isotope tracing using [3-^{13}C]serine, an 80 mg ml^{-1} solution of labeled serine was prepared in sterile 0.9% NaCl and kept at −20 °C until use. Mice were i.p. injected with 800 mg kg^{-1} of labeled serine 16 h before cell harvest by MACS. Mice were staggered in groups such that 4–6 mice were euthanized per hour. To identify metabolites with expected ^{13}C labeling, the mass of the extra neutron ($m = 1.00335$) was added to the expected m/z, enabling the calculation of percentage labeling for each carbon ($m+1$, $m+2$, $m+3$, etc.) corrected for natural abundance using IsoCorrectoR[67].

Histology and quantification

After isolation, mouse tissues were fixed for 24 h in 10% neutral buffered formalin, washed in deionized water and stored in 70% ethanol and 30% water until embedding. For mouse skulls, intact heads were fixed for 24 h, skinned and then fixed for another 24 h. All tissues were paraffin-embedded, sectioned and stained by hematoxylin and eosin by the Boston Children's Hospital Pathology Core.

For human COX IV staining, slides were stained using Abcam's IHC-P protocol with a 30-min antigen retrieval in sodium citrate buffer, using 10% goat serum in TBST for blocking and incubating overnight

in primary antibody in blocking buffer at 4 °C. Slides were incubated in secondary antibody in blocking buffer for 1 h at room temperature. DAPI (1 µg ml^{-1}) was added for one 5-min wash before mounting with ProLong Gold antifade mountant (Invitrogen, P36930).

Slides were imaged on a Zeiss Axio Imager.Z2 microscope (ZEN version 3.11). For COX IV quantification, 4–6 ×63 objective fields were acquired per tissue and the mean AF488 intensity was calculated on a per-tissue, per-mouse basis. All slides were imaged using the same acquisition settings (DAPI, 200 ms at 2%; AF488, 120 ms at 6%; AF594, 1,050 ms at 16%) and all immunofluorescence images were acquired in the same imaging session. One slide of tissue was analyzed per mouse. Slide labels were blinded using tape and randomized using a numeric code before imaging and quantitation and labels were relinked following quantitation. For per-cell AF488 signal, five cells were selected randomly per image and encircled using the spline contour function. Images selected for display in figures were exported from ZEN using identical display settings by tissue: spleen, AF488 range 30–255 nm, gamma = 1.0, DAPI range 29–107, gamma = 1.0; femurs and bone marrow, AF488 range 25–249 nm, gamma = 1.0, DAPI range 25–110, gamma = 1.0.

Statistics and reproducibility

All in vitro studies were set up as $n = 3$ biological replicates per experiment as default, with additional experimental replicates as indicated. For studies using mice, $n = 6$–8 mixed-sex littermates (at least three males and three females) were used per group at the beginning of the experiment. Mice were randomized on the basis of IVIS leukemia burden if available; otherwise, mice within the same cage were randomly assigned to each treatment group such that each group spanned multiple cages. No statistical method was used to predetermine sample size but our sample sizes are similar to those reported in previous publications[7,44,71]. Data distribution was assumed to be normal but this was not formally tested. For Seahorse data, wells were excluded if values did not show response to any of the injected drugs compared to the others within the same group. For mouse studies, outlier tests ($Q = 5\%$) were used in GraphPad Prism (version 10) for comparison of growth curves only; otherwise, all mice were included in statistical testing. Otherwise, no animals or data points were excluded from our experiments. Investigators were not blinded to group allocation for in vitro experiment or allocation during mouse experiments and outcome assessment. Investigators were blinded to histology results as described above. Analysis and visualization of metabolomics data (principal component analysis plots and volcano plots) were generated with MetaboAnalyst 5.0 (www.metaboanalyst.ca)[72]. Statistical analysis was performed using GraphPad Prism (version 10).

Reporting summary

Further information on research design is available in the Nature Portfolio Reporting Summary linked to this article.

Data availability

NGS data for the barcoding experiment and in vivo CRISPR screen were deposited to the Sequence Read Archive under BioProject PRJNA1447583. All metabolomics data are available from the NIH Common Fund's NMDR, the Metabolomics Workbench (https://www.metabolomicsworkbench.org), where it has been assigned project identifier PR002390 (https://doi.org/10.21228/M8Q250). Data for survival analyses were obtained from the NIH Genomic Data Commons (https://portal.gdc.cancer.gov/projects/TARGET-ALL-P2, https://portal.gdc.cancer.gov/projects/MP2PRT-ALL) and from Xena (https://xenabrowser.net/). Other data and materials that support the findings of this study are available from the corresponding author upon request. Source data are provided with this paper.

Code availability

R scripts used for formatting and normalization of metabolomics datasets can be found on GitHub (https://github.com/FrozenGas/KanarekLabTraceFinderRScripts).

References

1. Remsik, J. & Boire, A. The path to leptomeningeal metastasis. *Nat. Rev. Cancer* **24**, 448–460 (2024).
2. Thastrup, M., Duguid, A., Mirian, C., Schmiegelow, K. & Halsey, C. Central nervous system involvement in childhood acute lymphoblastic leukemia: challenges and solutions. *Leukemia* **36**, 2751–2768 (2022). 1–18.
3. Sison, E. A. R. & Silverman, L. B. CNS prophylaxis in pediatric acute lymphoblastic leukemia. *Hematology* **2014**, 198–201 (2014).
4. Rheingold, S. R. et al. Determinants of survival after first relapse of acute lymphoblastic leukemia: a Children's Oncology Group study. *Leukemia* **38**, 2382–2394 (2024).
5. Cheung, Y. T. et al. Leukoencephalopathy and long-term neurobehavioural, neurocognitive, and brain imaging outcomes in survivors of childhood acute lymphoblastic leukaemia treated with chemotherapy: a longitudinal analysis. *Lancet Haematol.* **3**, e456–e466 (2016).
6. Hunger, S. P. & Mullighan, C. G. Acute lymphoblastic leukemia in children. *N. Engl. J. Med.* **373**, 1541–1552 (2015).
7. Kanarek, N. et al. Histidine catabolism is a major determinant of methotrexate sensitivity. *Nature* **559**, 632–636 (2018).
8. Bhojwani, D. et al. Methotrexate-induced neurotoxicity and leukoencephalopathy in childhood acute lymphoblastic leukemia. *J. Clin. Oncol.* **32**, 949–959 (2014).
9. Mateos, M. K. et al. Methotrexate-related central neurotoxicity: clinical characteristics, risk factors and genome-wide association study in children treated for acute lymphoblastic leukemia. *Haematologica* **107**, 635–643 (2022).
10. Gibson, E. M. et al. Methotrexate chemotherapy induces persistent tri-glial dysregulation that underlies chemotherapy-related cognitive impairment. *Cell* **176**, 43–55 (2019).
11. Jang, A. et al. Choroid plexus–CSF-targeted antioxidant therapy protects the brain from toxicity of cancer chemotherapy. *Neuron* **110**, 3288–3301 (2022).
12. Abbott, K. L. et al. Nutrient requirements of organ-specific metastasis in breast cancer. *Nature* **649**, 1292–1301 (2026).
13. Frishman-Levy, L. & Izraeli, S. Advances in understanding the pathogenesis of CNS acute lymphoblastic leukaemia and potential for therapy. *Br. J. Haematol.* **176**, 157–167 (2017).
14. Ngo, B. et al. Limited environmental serine and glycine confer brain metastasis sensitivity to PHGDH inhibition. *Cancer Discov.* **10**, 1352–1373 (2020).
15. Savino, A. M. et al. Metabolic adaptation of acute lymphoblastic leukemia to the central nervous system microenvironment depends on stearoyl-CoA desaturase. *Nat. Cancer* **1**, 998–1009 (2020).
16. Ferraro, G. B. et al. Fatty acid synthesis is required for breast cancer brain metastasis. *Nat. Cancer* **2**, 414–428 (2021).
17. Roberts, K. G. & Mullighan, C. G. Genomics in acute lymphoblastic leukaemia: insights and treatment implications. *Nat. Rev. Clin. Oncol.* **12**, 344–357 (2015).
18. Chow, R. D. & Chen, S. Cancer CRISPR screens in vivo. *Trends Cancer* **4**, 349–358 (2018).
19. Passaro, D. et al. CXCR4 is required for leukemia-initiating cell activity in T cell acute lymphoblastic leukemia. *Cancer Cell* **27**, 769–779 (2015).
20. Maryon, E. B., Molloy, S. A. & Kaplan, J. H. Cellular glutathione plays a key role in copper uptake mediated by human copper transporter 1. *Am. J. Cell Physiol.* **304**, 768–779 (2013).

21. Ge, E. J. et al. Connecting copper and cancer: from transition metal signalling to metalloplasia. *Nat. Rev. Cancer* **22**, 102–113 (2022).
22. Ramchandani, D. et al. Copper depletion modulates mitochondrial oxidative phosphorylation to impair triple negative breast cancer metastasis. *Nat. Commun.* **12**, 7311 (2021).
23. Nengroo, M. A. et al. Accumulation of succinate suppresses de novo purine synthesis through succinylation-mediated control of the mitochondrial folate cycle. *Mol. Cell* **85**, 4215–4228 (2025).
24. Joergstuerenburg, H., Oechsner, M., Schroeder, S. & Kunze, K. Determinants of the copper concentration in cerebrospinal fluid. *J. Neurol. Neurosurg. Psychiatry* **67**, 252–253 (1999).
25. Kaiafa, G. D. et al. Copper levels in patients with hematological malignancies. *Eur. J. Intern. Med.* **23**, 738–741 (2012).
26. Tessmer, C. F., Hrgovcic, M., Brown, B. W., Wilbur, J. & Thomas, F. B. Serum copper correlations with bone marrow. *Cancer* **29**, 173–179 (1972).
27. Carpentieri, U., Myers, J., Thorpe, L., Daeschner, C. W. 3rd & Haggard, M. E. Copper, zinc, and iron in normal and leukemic lymphocytes from children. *Cancer Res.* **46**, 981–984 (1986).
28. Dobson, S. M. et al. Relapse fated latent diagnosis subclones in acute B lineage leukaemia are drug tolerant and possess distinct metabolic programs. *Cancer Discov.* **10**, 568–587 (2020).
29. Vanner, R. J. et al. Multiomic profiling of central nervous system leukemia identifies mRNA translation as a therapeutic target. *Blood Cancer Discov.* **3**, 16–31 (2022).
30. Dotevall, L. & Hagberg, L. Penetration of doxycycline into cerebrospinal fluid in patients treated for suspected Lyme neuroborreliosis. *Antimicrob. Agents Chemother.* **33**, 1078–1080 (1989).
31. Heath, A. P. et al. The NCI Genomic Data Commons. *Nat. Genet.* **53**, 257–262 (2021).
32. Kim, B.-E., Nevitt, T. & Thiele, D. J. Mechanisms for copper acquisition, distribution and regulation. *Nat. Chem. Biol.* **4**, 176–185 (2008).
33. Kar, S. et al. Copper(II) import and reduction are dependent on His–Met clusters in the extracellular amino terminus of human copper transporter-1. *J. Biol. Chem.* **298**, 101631 (2022).
34. Petris, M. J., Smith, K., Lee, J. & Thiele, D. J. Copper-stimulated endocytosis and degradation of the human copper transporter, hCtr1. *J. Biol. Chem.* **278**, 9639–9646 (2003).
35. Curnock, R. & Cullen, P. J. Mammalian copper homeostasis requires retromer-dependent recycling of the high-affinity copper transporter 1. *J. Cell Sci.* **133**, jcs249201 (2020).
36. Chun, H., Catterton, T., Kim, H., Lee, J. & Kim, B.-E. Organ-specific regulation of ATP7A abundance is coordinated with systemic copper homeostasis. *Sci. Rep.* **7**, 12001 (2017).
37. Vest, K. E., Paskavitz, A. L., Lee, J. B. & Padilla-Benavides, T. Dynamic changes in copper homeostasis and post-transcriptional regulation of Atp7a during myogenic differentiation. *Metallomics* **10**, 309–322 (2018).
38. Poursani, E. M. et al. Copper chelation suppresses epithelial–mesenchymal transition by inhibition of canonical and non-canonical TGF-β signaling pathways in cancer. *Cell Biosci.* **13**, 132 (2023).
39. Ma, M. et al. Establishment of a specific in vivo Cu(I) reporting system based on metallothionein screening. *Metallomics* **13**, mfab035 (2021).
40. Bischoff, M. E. et al. Copper drives remodeling of metabolic state and progression of clear cell renal cell carcinoma. *Cancer Discov.* **15**, 401–426 (2025).
41. Chen, D. et al. An improved bathocuproine assay for accurate valence identification and quantification of copper bound by biomolecules. *Anal. Biochem.* **497**, 27–35 (2016).
42. Furukawa, Y., Torres, A. S. & O'Halloran, T. V. Oxygen-induced maturation of SOD1: a key role for disulfide formation by the copper chaperone CCS. *EMBO J.* **23**, 2872–2881 (2004).
43. Brady, D. C. et al. Copper is required for oncogenic BRAF signaling and tumorigenesis. *Nature* **509**, 492–496 (2014).
44. Martínez-Reyes, I. et al. Mitochondrial ubiquinol oxidation is necessary for tumor growth. *Nature* **585**, 288–292 (2020).
45. Glasauer, A., Sena, L. A., Diebold, L. P., Mazar, A. P. & Chandel, N. S. Targeting SOD1 reduces experimental non-small-cell lung cancer. *J. Clin. Invest.* **124**, 117–128 (2014).
46. Liberti, M. V. & Locasale, J. W. The Warburg effect: how does it benefit cancer cells? *Trends Biochem. Sci* **41**, 211 (2016).
47. Birsoy, K. et al. An essential role of the mitochondrial electron transport chain in cell proliferation is to enable aspartate synthesis. *Cell* **162**, 540–551 (2015).
48. Sullivan, L. B. et al. Aspartate is an endogenous metabolic limitation for tumour growth. *Nat. Cell Biol.* **20**, 782–788 (2018).
49. Wu, Z. et al. Electron transport chain inhibition increases cellular dependence on purine transport and salvage. *Cell Metab.* **36**, 1504–1520 (2024).
50. Tran, D. H. et al. De novo and salvage purine synthesis pathways across tissues and tumors. *Cell* **187**, 3602–3618 (2024).
51. Alvarez, H. M. et al. Tetrathiomolybdate inhibits copper trafficking proteins through metal cluster formation. *Science* **327**, 331–334 (2009).
52. Brewer, G. J. Zinc acetate for the treatment of Wilson's disease. *Expert Opin. Pharmacother.* **2**, 1473–1477 (2001).
53. Anderson, L. A., Hakojarvi, S. L. & Boudreaux, S. K. Zinc acetate treatment in Wilson's disease. *Ann. Pharmacother.* **32**, 78–87 (1998).
54. Chan, N. et al. Influencing the tumor microenvironment: a phase II study of copper depletion using tetrathiomolybdate in patients with breast cancer at high risk for recurrence and in preclinical models of lung metastases. *Clin. Cancer Res.* **23**, 666–676 (2017).
55. Mehdi, W. A. et al. Effects of acute lymphoblastic leukemia on ceruloplasmin oxidase, copper and several markers of oxidative damage, in children. *Asian Pac. J. Cancer Prev.* **16**, 5205–5210 (2015).
56. Goldstein, I. M., Kaplan, H. B., Edelson, H. S. & Weissmann, G. Ceruloplasmin: an acute phase reactant that scavenges oxygen-derived free radicals. *Ann. N. Y. Acad. Sci.* **389**, 368–379 (1982).
57. Fujisawa, C. et al. Early clinical signs and treatment of Menkes disease. *Mol. Genet. Metab. Rep.* **31**, 100849 (2022).
58. Tsang, T. et al. Copper is an essential regulator of the autophagic kinases ULK1/2 to drive lung adenocarcinoma. *Nat. Cell Biol.* **22**, 412–424 (2020).
59. Newton, S. E. B. et al. ER stress tolerance is regulated by copper-dependent PERK kinase activity. *Cell Rep.* **44**, 116318 (2025).
60. Guo, J. et al. Copper promotes tumorigenesis by activating the PDK1–AKT oncogenic pathway in a copper transporter 1 dependent manner. *Adv. Sci.* **8**, 2004303 (2021).
61. Kramer, N. J. et al. Regulators of mitonuclear balance link mitochondrial metabolism to mtDNA expression. *Nat. Cell Biol.* **25**, 1575–1589 (2023).
62. Maynard, A. G. et al. Folate depletion induces erythroid differentiation through perturbation of de novo purine synthesis. *Sci. Adv.* **10**, eadj9479 (2024).
63. Salabei, J. K., Gibb, A. A. & Hill, B. G. Comprehensive measurement of respiratory activity in permeabilized cells using extracellular flux analysis. *Nat. Protoc.* **9**, 421–438 (2014).
64. Petrova, B. et al. Redox metabolism measurement in mammalian cells and tissues by LC–MS. *Metabolites* **11**, 313 (2021).

65. Doench, J. G. et al. Optimized sgRNA design to maximize activity and minimize off-target effects of CRISPR–Cas9. *Nat. Biotechnol.* **34**, 184–191 (2016).
66. Sanson, K. R. et al. Optimized libraries for CRISPR–Cas9 genetic screens with multiple modalities. *Nat. Commun.* **9**, 5416 (2018).
67. Heinrich, P. et al. Correcting for natural isotope abundance and tracer impurity in MS-, MS/MS- and high-resolution-multiple-tracer-data from stable isotope labeling experiments with IsoCorrectoR. *Sci. Rep.* **8**, 17910 (2018).
68. Goldman, M. J. et al. Visualizing and interpreting cancer genomics data via the Xena platform. *Nat. Biotechnol.* **38**, 675–678 (2020).
69. Dwivedi, B., Mumme, H., Satpathy, S., Bhasin, S. S. & Bhasin, M. Survival Genie, a web platform for survival analysis across pediatric and adult cancers. *Sci. Rep.* **12**, 3069 (2022).
70. Townsend, E. C. et al. The Public Repository of Xenografts enables discovery and randomized phase II-like trials in mice. *Cancer Cell* **29**, 574–586 (2016).
71. Jin, Q. et al. Oncogenic deubiquitination controls tyrosine kinase signaling and therapy response in acute lymphoblastic leukemia. *Sci. Adv.* **8**, eabq8437 (2022).
72. Pang, Z. et al. MetaboAnalyst 6.0: towards a unified platform for metabolomics data processing, analysis and interpretation. *Nucleic Acids Res.* https://doi.org/10.1093/nar/gkae253 (2024).

Acknowledgements

We acknowledge the contributions of the participants and families without whom this research would not be possible. We thank the Animal Research at Children's facility at Boston Children's Hospital for their support with animal work and the Boston Children's Hospital Histology Department for their support with tissue sectioning and staining. We also thank the Boston Children's Hospital Hematology/Oncology and Harvard Stem Cell Institute Flow Cytometry Research Laboratory for their services, as well as the Genomic Perturbation Platform at the Broad Institute. We acknowledge M. Schwartz (Broad institute) for the contribution of the barcoding library, A. Gutierrez (Boston Children's Hospital) for his advice and for providing some of the cell lines used in this study and N. Chandel (Northwestern University) for contributing several plasmids used in this study. We acknowledge J. Perry (Dana-Farber Cancer Institute) for her assistance with procuring the PDX samples. Additionally, we thank J. Ubellacker (Harvard School of Public Health) and D. Langenau (Massachusetts General Hospital) for their advice.

Author contributions

Conceptualization, A.Y.L.W., N.K., D.C.B., P.W., A.Y., N.K.P. and G.P. Methodology, D.C.B., R.W., P.D.C., J.W.M., G.P. and L.B.S. Investigation, A.Y.L.W., A.G.M., J.R.B., B.P., C.M., M.D.S., J.W.M., B.B., G.P. and M.W. Visualization, A.Y.L.W., J.W.M., B.P. and G.P. Funding acquisition, A.Y.L.W. and N.K. Project administration, N.K., D.C.B., K.S. and L.S.C. Supervision, N.K. Writing—original draft, A.Y.L.W. and N.K. Writing—review and editing, all authors.

Funding

We acknowledge the following funding sources: Metabolomics Workbench/National Metabolomics Data Repository (NMDR; grant U2C-DK119886), Common Fund Data Ecosystem (grant 3OT2OD030544), Metabolomics Consortium Coordinating Center (grant 1U2C-DK119889), Harvard Digestive Disease Center and the NIH (grant P30DK034854), BCH Cellular Imaging Core (RRID:SCR_026485), funded by the NIH (P50 HD105351), Doctoral Foreign Studies Award from the Canadian Institutes of Health Research (DFD-181606, to A.Y.W.), Predoctoral Fellowship in Drug Discovery 2025 from the PhRMA Foundation (A.Y.W.), Gabrielle's Angels Foundation for Cancer Research (N.K.), NIH National Cancer Institute (R01 CA282477-01A1 and R01 CA279550-01, to N.K.), NIH National Institute on Aging (R21AG091645, to G.P. and L.S.C.), STARR Cancer Consortium Research Grant (N.K.), Smith Family Awards Program for Excellence in Biomedical Research (N.K.), Croucher Foundation (P.W.), National Science Foundation Graduate Research Fellowship Program 2023 Fellowship (A.Y.), NIH (F31 1F31HL178310, to N.K.P.), NIH National Institute of General Medical Sciences (5R35GM124749, to D.C.B), Ludwig Princeton Branch (D.C.B.) and Pew Charitable Trusts Biomedical Science Innovation Fund (D.C.B.). K.S. received support from Team Crank and the Children's Leukemia Research. N.K. is a Pew Scholar. The funders had no role in study design, data collection and analysis, decision to publish or preparation of the manuscript.

Competing interests

A.Y.W. and N.K. hold a provisional patent application (37314-0156P01) for the use of copper-depleting therapies to boost the effect of chemotherapy. D.C.B. holds ownership in Merlon and Elaeis Therapeutics. L.B.S. served on an advisory board for Servier Pharmaceuticals and serves as a consultant and on an advisory board and speaker's bureau for Jazz Pharmaceuticals. D.C.B. is an inventor on patent application 20150017261 entitled 'Methods of treating and preventing cancer by disrupting the binding of copper in the MAP kinase pathway'. K.S. is a member of the scientific advisory board and has stock options with Auron Therapeutics on topics unrelated to the work. The other authors declare no competing interests.

Additional information

Extended data is available for this paper at https://doi.org/10.1038/s43018-026-01177-4.

Supplementary information The online version contains supplementary material available at https://doi.org/10.1038/s43018-026-01177-4.

Correspondence and requests for materials should be addressed to Naama Kanarek.

Peer review information *Nature Cancer* thanks Issam Ben-Sahra, Navdeep Chandel and the other, anonymous, reviewer(s) for their contribution to the peer review of this work. Peer reviewer reports are available.

[1]Harvard/MIT MD-PhD Program, Harvard Medical School, Boston, MA, USA. [2]Harvard Medical School, Boston, MA, USA. [3]Department of Pathology, Boston Children's Hospital, Boston, MA, USA. [4]Broad Institute of MIT and Harvard, Boston, MA, USA. [5]Department of Genetics, Blavatnik Institute, Harvard Medical School, Boston, MA, USA. [6]Core Facilities, Medical University of Vienna, Vienna, Austria. [7]Department of Cancer Biology, Perelman School of Medicine, University of Pennsylvania, Philadelphia, PA, USA. [8]Harvard T. H. Chan School of Public Health, Boston, MA, USA. [9]Department of Pediatric Oncology, Dana-Farber Cancer Institute and Division of Pediatric Hematology-Oncology, Boston Children's Hospital, Boston, MA, USA. [10]Department of Pediatrics, Rutgers Cancer Institute, Rutgers Robert Wood Johnson Medical School, New Brunswick, NJ, USA. [11]Abramson Family Cancer Research Institute, Perelman School of Medicine, University of Pennsylvania, Philadelphia, PA, USA. ✉e-mail: naama.kanarek@childrens.harvard.edu

https://doi.org/10.1038/s43018-026-01177-4

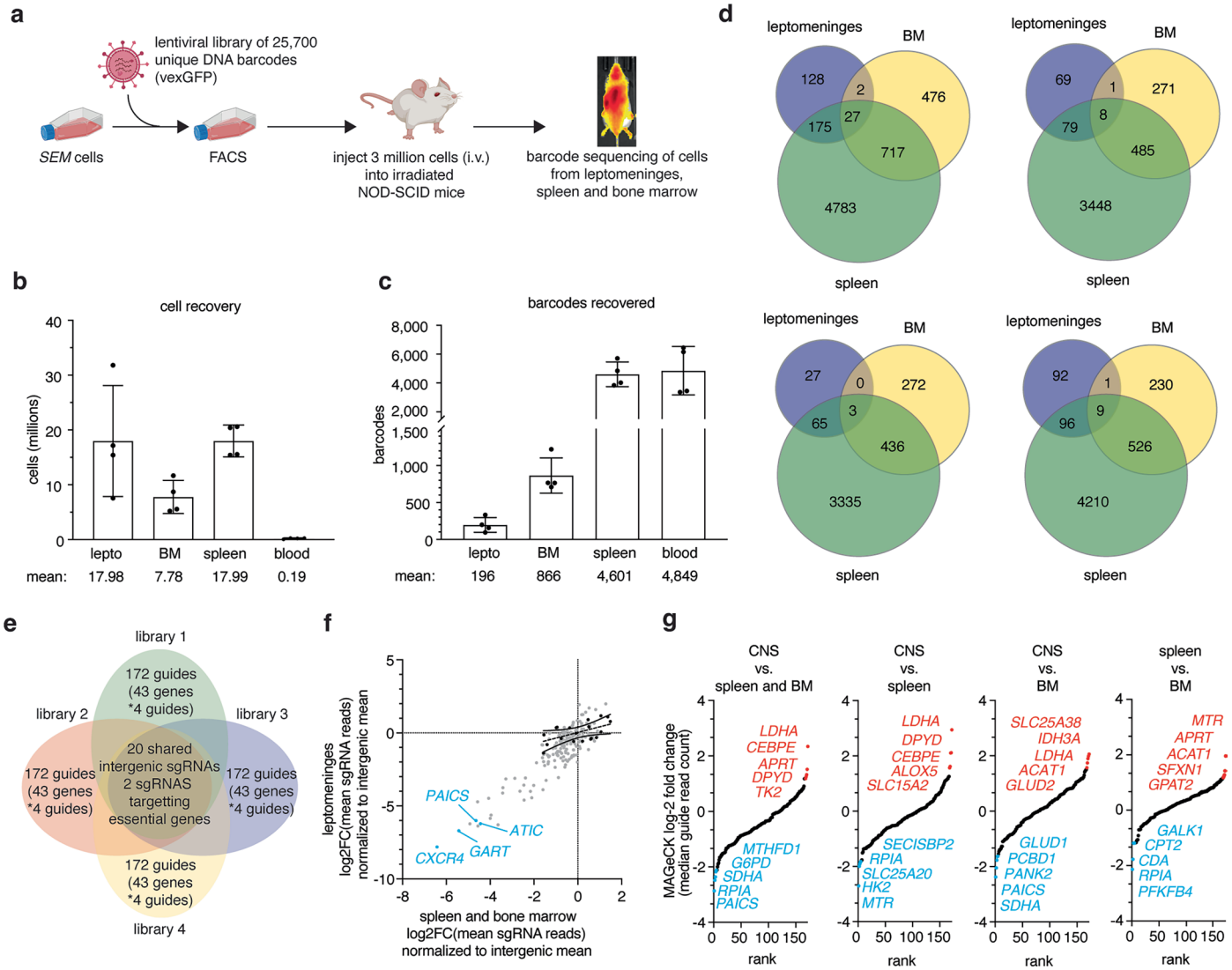

Extended Data Fig. 1 | In vivo CRISPR screen identifies organ-specific metabolic vulnerabilities. (**a**) Overview of barcoding experiment. i.v. = intravenous. Created in BioRender and further modified in Illustrator. Wong, A. (2026) https://BioRender.com/6t8alxv. (**b**) Total cell recovery by organ in millions as determined by manual counting with a hemocytometer and staining with trypan blue. Each dot represents an individual mouse, $n = 4$ mice. lepto = leptomeninges, BM = bone marrow. (**c**) Total number of barcodes recovered from each organ per mouse as determined by next-generation sequencing. The number of barcodes recovered from an organ was determined by the number of barcodes summing up to 90% of total reads from each sample. $n = 4$ mice per group. (**d**) Venn diagrams (1 per mouse) illustrating unique and shared barcodes across organs within each mouse. (**e**) An overview of CRISPR library design. (**f**) CRISPR screen results. Grey dots represent genes in screen, black dots represent intergenic guideRNAs with linear regression and 99% confidence band overlaid. Blue dots represent known ALL dependencies. Axes represent mean log(2) fold change of the MAGeCK-normalized read counts of guides for each gene, relative to the mean read counts of the intergenic guides. (**g**) Genes from the CRISPR screen are ranked by relative depletion or enrichment in one organ versus another. The 5 most depleted (blue) or enriched (red) genes are highlighted in each plot. CNS = central nervous system, BM = bone marrow.

https://doi.org/10.1038/s43018-026-01177-4

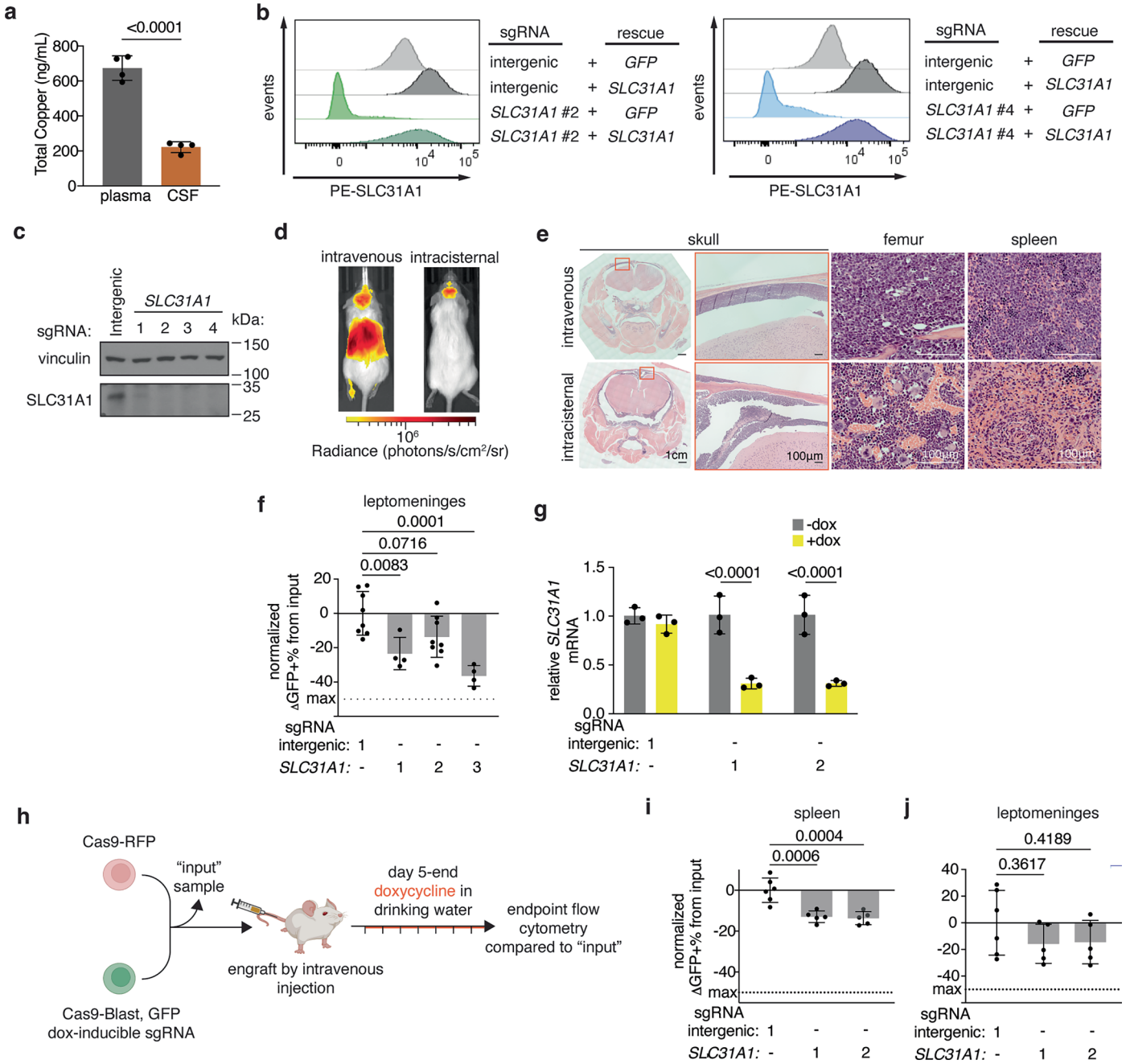

Extended Data Fig. 2 | Knockout of *SLC31A1* inhibits growth of ALL in vivo. (**a**) Total copper levels in the plasma and cerebrospinal fluid (CSF) of untreated NOD-SCID mice as measured by inductively-coupled plasma mass spectrometry (ICP-MS). $n = 4$ mice per group. P value from two-sided paired t-test. (**b**) Flow cytometric assessment of *SLC31A1* expression using indirect antibody staining in live SEM cells with knockout of *SLC31A1* with GFP or CRISPR-resistant SLC31A1 rescue. Representative data from two experiments shown. (**c**) Immunoprecipitation-western blot validation of *SLC31A1* knockout. This experiment was performed once. (**d**) Representative bioluminescent imaging (BLI) of mice 3 weeks after receiving luciferase-expressing SEM cells by either intravenous or intracisternal injection. (**e**) Hematoxylin and eosin staining of sections from skulls, spleens and femurs of terminal mice receiving luciferase-expressing SEM cells by intravenous or intracisternal injection. Scale bar for whole-skull images are 1 cm, all other scale bars (including skull inset images) are 100 micrometers. Orange rectangles denote inset of skull images. Representative images from a single experiment containing 3 mice in each group are shown. (**f**) Change in %GFP+ cells compared to input, from CNS of mice at clinical endpoint that received intergenic or SLC31A1-KO sgRNA cells mixed with control mCherry-expressing cells by intravenous injection. Data are normalized to the mean of the intergenic group. $n = 8$ intergenic, 4 guide #1, 8 guide #2, 4 guide #3 mice. Data represent the combination of two independent replicates of the experiment with different guides. P values from two-sided Šídák's multiple comparisons test adjusted for multiple comparisons. (**g**) Quantitative real-time polymerase chain reaction (qRT-PCR) measurement of SLC31A1 mRNA knockdown following doxycycline-inducible sgRNA expression. mRNA was collected from cells after 9 days of doxycycline induction. Each group is normalized to the -doxycycline condition. $n = 3$ biological replicates per group. P values from two-sided Šídák's multiple comparisons test adjusted for multiple comparisons. (**h**) Experimental setup of in vivo mixing experiment in which doxycycline was administered via the drinking water starting at day 5 post engraftment. Created in BioRender and further modified in Illustrator. Wong, A. (2026) https://BioRender.com/mgcs6yq. (**i-j**) Change in %GFP+ cells compared to input, from mice at clinical endpoint that received intergenic or SLC31A1-KO sgRNA cells mixed with control mCherry-expressing cells. Data are normalized to the mean of the intergenic group and are from the (**i**) spleen or (**j**) CNS of mice receiving cells by intravenous injection. For (**i**), $n = 6$ intergenic mice, 5 guide #1, 5 guide #2; for (**j**), 6 intergenic, 5 guide #1, 5 guide #2 mice. Each dot represents an individual mouse. P values from two-sided Šídák's multiple comparisons test adjusted for multiple comparisons. Plotted data are mean ± SD. P values from two-sided Šídák's multiple comparisons test adjusted for multiple comparisons.

https://doi.org/10.1038/s43018-026-01177-4

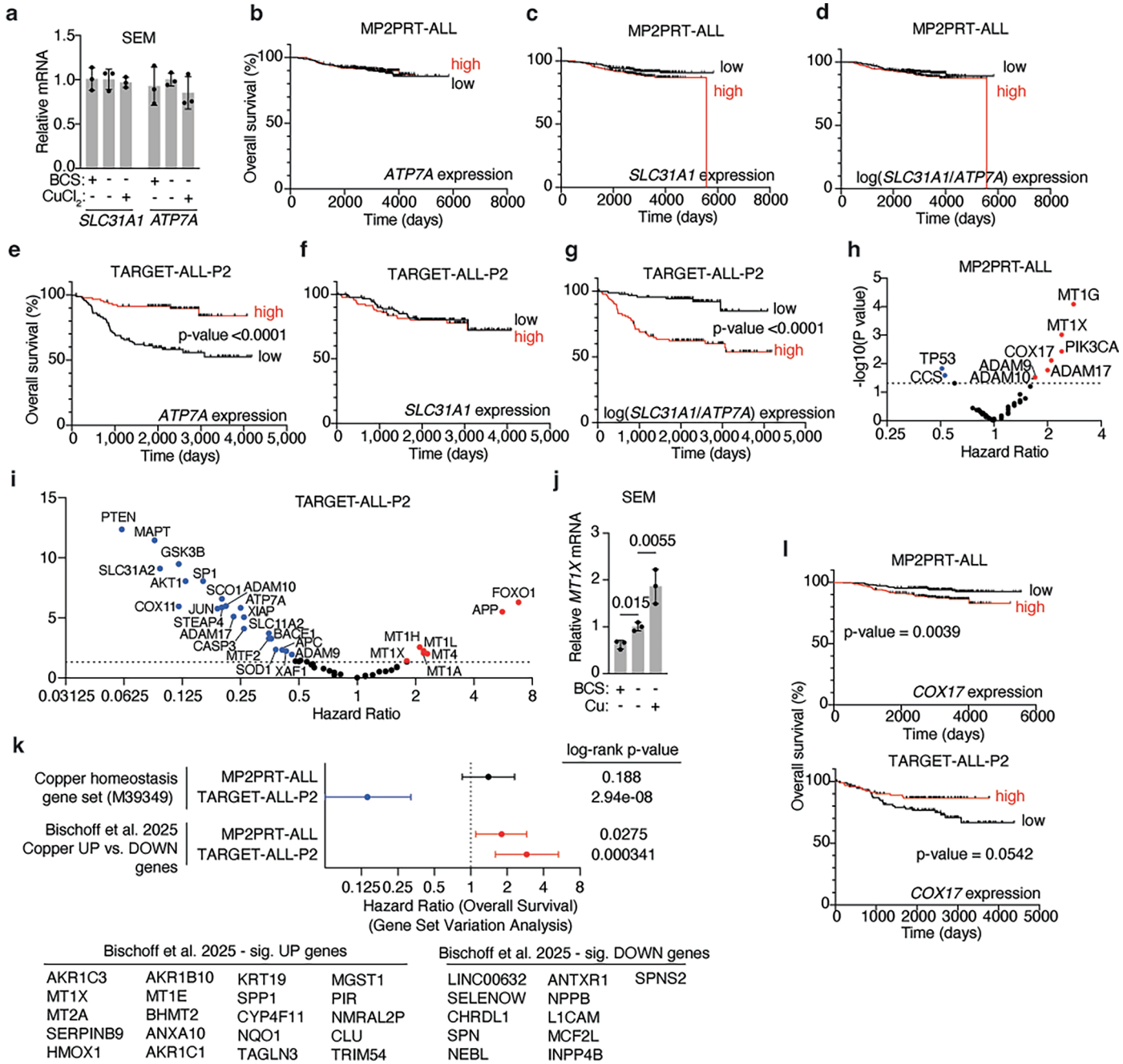

Bischoff et al. 2025 - sig. UP genes

AKR1C3	AKR1B10	KRT19	MGST1
MT1X	MT1E	SPP1	PIR
MT2A	BHMT2	CYP4F11	NMRAL2P
SERPINB9	ANXA10	NQO1	CLU
HMOX1	AKR1C1	TAGLN3	TRIM54

Bischoff et al. 2025 - sig. DOWN genes

LINC00632	ANTXR1	SPNS2
SELENOW	NPPB	
CHRDL1	L1CAM	
SPN	MCF2L	
NEBL	INPP4B	

Extended Data Fig. 3 | Analysis of MP2PRT-ALL and TARGET-ALL survival data. (**a**) qRT-PCR measurement of SLC31A1 or ATP7A mRNA levels in 8-day BCS or $CuCl_2$ treated SEM cells relative to vehicle treated cells. $n = 3$ biological replicates per condition. Cells were treated with 50 μM BCS or $CuCl_2$. (**b-g**) Kaplan-Meier survival curves of patients from MPT2PRT-ALL or TARGET-ALL-P2 cohorts with available bone marrow mRNA-sequencing and overall survival (OS) data, vertical dashes represent censored patients. Patients ($n = 374$ for TARGET, 1,290 for MP2PRT-ALL) were sorted by (**b, e**) ATP7A, (**c, f**) SLC31A1, or (**d, g**) log(SLC31A1/ATP7A) expression in transcripts per million (TPM), and the survival data of the top ('high') and bottom quartiles ('low') were plotted. (**h-i**) Volcano plot of hazard ratios of copper homeostasis genes (GSEA M39349) comparing survival of the top and bottom quartiles ($n = 311$ per quartile for MP2PRT-ALL, and $n = 95$ per quartile for TARGET-ALL-P2) of patients based on expression. Log-rank *P* values and hazard ratios calculated using SurvivalGenie 2.0. Data presented from bone marrow samples of patients in the (**h**) MP2PRT-ALL or (**i**) TARGET-ALL-P2 cohorts. (**j**) qRT-PCR measurement of MT1X mRNA levels in 8-day 50 μM BCS or $CuCl_2$ treated SEM cells relative to vehicle treated cells. $n = 3$ biological replicates per condition. *P* value from two-sided Dunnett's multiple comparisons test adjusted for multiple comparison. (**k**) Hazard ratios of top and bottom quartiles of MP2PRT-ALL and TARGET-ALL-P2 patients using gene set variation analysis (GSVA) for either copper homeostasis genes (GSEA M39349), or GSVA contrasting up-regulated vs. down-regulated genes (adjusted *P* value <0.05) in response to copper treatment from Bischoff et al. 2025. Log-rank *P* values and hazard ratios calculated using SurvivalGenie 2.0. Up-regulated and down-regulated genes are listed below. Plotted value is the hazard ratio with the 95% confidence interval. (**l**) Kaplan-Meier survival curves of patients from MPT2PRT-ALL or TARGET-ALL-P2 cohorts sorted by COX17 expression with the top and bottom quartiles plotted. *P* values from log-rank (Mantel-Cox) tests or (**j**) Dunnett's multiple comparisons test. sig. = significant, n.s. = not significant.

https://doi.org/10.1038/s43018-026-01177-4

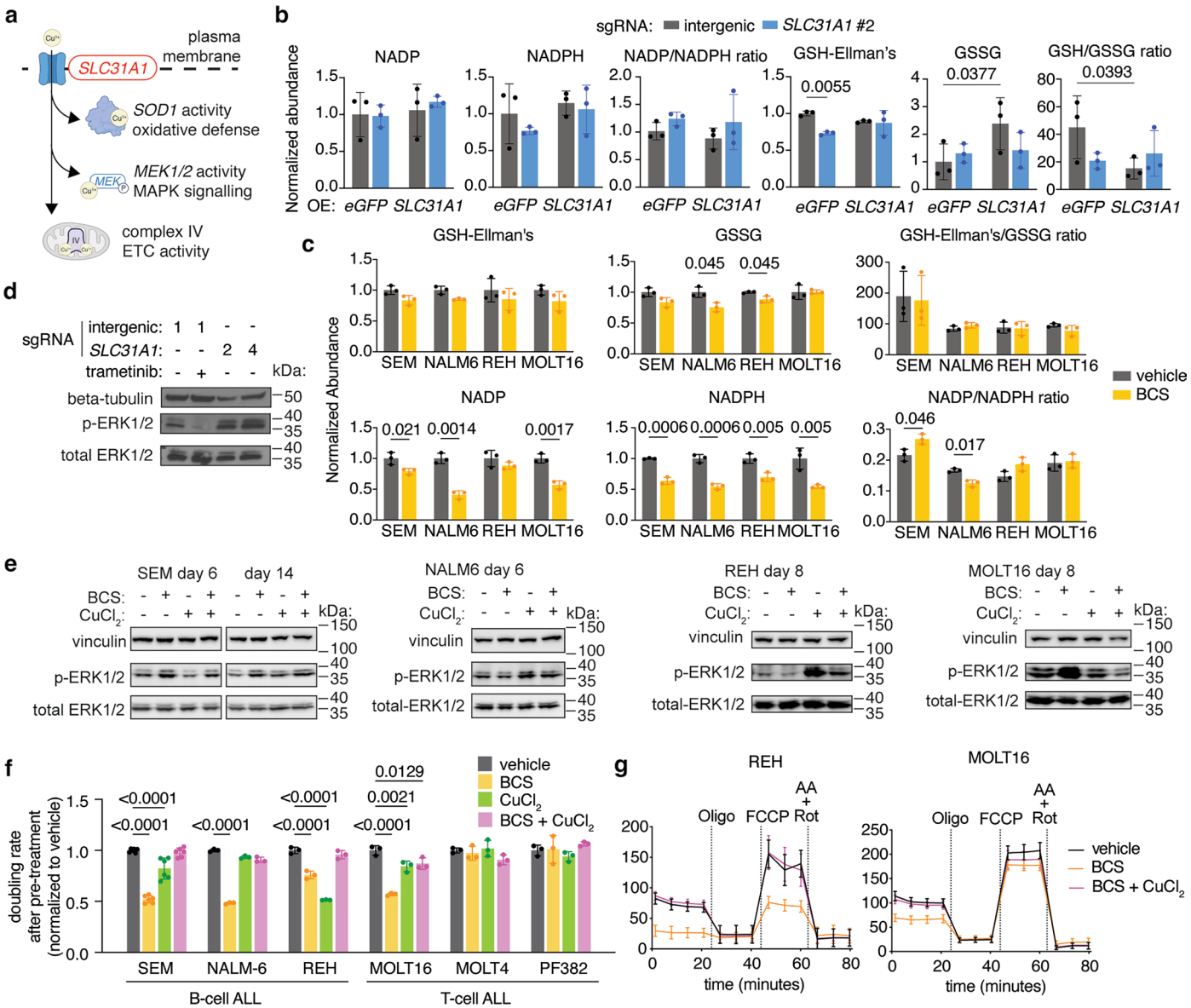

Extended Data Fig. 4 | Copper depletion does not significantly affect baseline NADP/NADPH levels, glutathione ratios nor hinder MAPK signaling in ALL cells in vitro. (**a**) A scheme illustrating primary intracellular functions of copper ions. (**b-c**) NADP, NADPH levels and NADP/NADPH ratio, as well as oxidized and reduced glutathione levels as determined by LC-MS targeted metabolite profiling in (**b**) SLC31A1-KO SEM cells with or without genetic rescue, or (**c**) BCS-treated SEM cells (day 14), NALM6 (day 6), REH (day 8) or MOLT16 (day 8) with or without $CuCl_2$ rescue. Levels of reduced glutathione were determined by derivatization with Ellman's reagent. $n = 3$ biological replicates per condition. P values from two-sided Šídák's multiple comparisons test adjusted for multiple comparisons. (**d-e**) Western blotting for total and phospho (p-)ERK1/2 levels in (**d**) SLC31A1-KO or (**e**) BCS treated SEM, NALM6, REH or MOLT16 cells. Each cell line was tested in biological triplicates and a representative replicate is shown. (**f**) Doublings per day normalized to vehicle-treated cells after either 4 days (NALM6) or 6 days of 50 μM BCS pre-treatment (SEM, REH, MOLT16, MOLT4, PF382). BCS treatment was continued after the pre-treatment period. Doubling rate was calculated by taking the linear regression of cell number across at least 2 passages over 4 days. $n = 3$ biological replicates per condition. P values from two-sided Šídák's multiple comparisons test adjusted for multiple comparisons. (**g**) MitoStress Seahorse Assay for indicated cell lines treated with BCS and/or $CuCl_2$ after 10 days of treatment. $n = 4$ biological replicates (wells) for each condition are plotted per timepoint. All other plotted data are mean ± SD, P values from two-sided Šídák's multiple comparisons test adjusted for multiple comparisons. Each dot represents a biological replicate. OE = overexpression, sgRNA = single guide RNA, oligo = oligomycin, AA = antimycin A, Rot = rotenone, FCCP = carbonyl cyanide-p-trifluoromethoxyphenylhydrazone.

https://doi.org/10.1038/s43018-026-01177-4

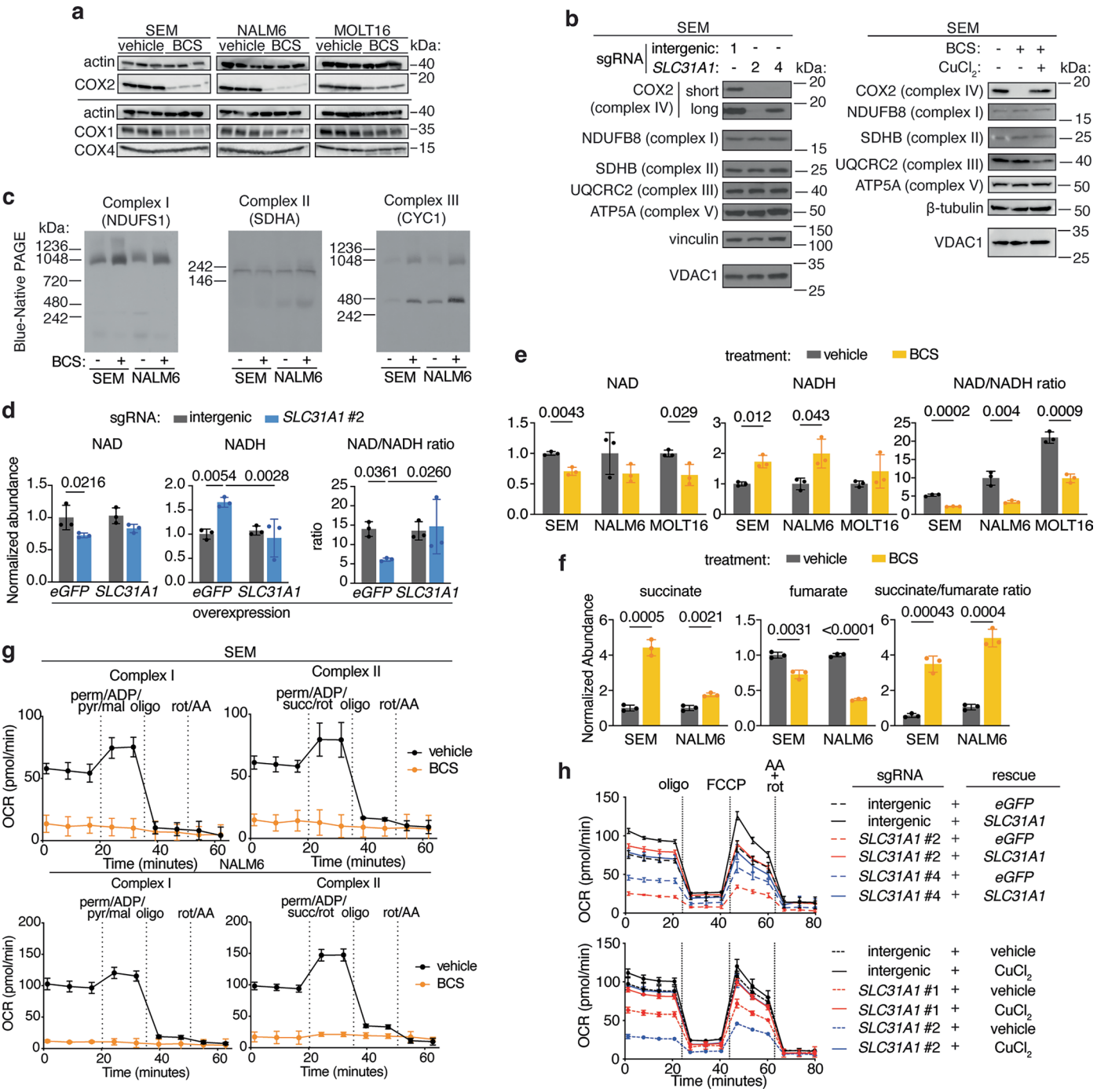

Extended Data Fig. 5 | Copper depletion disrupts complex IV and perturbs ETC activity. (**a**) Reducing and denaturing western blot for COX2, COX1 and COX4 in BCS-treated SEM (day 8), NALM6 (day 6) and MOLT16 (day 8) cells. Each lane represents an independent biological replicate (total 3 replicates). (**b**) Reduced and denaturing western blot assessment of subunits from the listed respiratory complexes of (left) SLC31A1-KO SEM cells or (right) day 8 BCS-treated SEM cells. Representative data is shown from 3 biological replicates per condition. (**c**) Blue-native (BN-PAGE) followed by western blot detection of indicated subunits in native complex I-III in BCS treated SEM cells (day 8) or NALM6 cells (day 6). Representative data of two biological replicates shown. Additional replicate shown in Source Data. (**d-e**) Levels of NAD, NADH and the NAD/NADH ratio were determined by LC-MS targeted metabolite profiling in (**d**) SLC31A1-KO SEM cells or (**e**) BCS treated SEM (day 8), NALM6 (day 6) and MOLT16 (day 8) cells. $n = 3$ biological replicates per condition. P values from two-sided Šídák's multiple comparisons test adjusted for multiple comparisons. (**f**) Levels of succinate, fumarate, and succinate/fumarate ratio in BCS treated SEM and NALM6 cells as determined by targeted LC-MS metabolite profiling. $n = 3$ biological replicates per condition. P values from two-sided Šídák's multiple comparisons test adjusted for multiple comparisons. (**g**) Seahorse assay to measure OCR in permeabilized BCS-treated SEM (day 8) or NALM6 (day 6) cells following treatment with complex I or II substrates. $n = 4$ biological replicates (wells) for each condition are plotted per timepoint. (**h**) MitoStress Seahorse assay performed on SLC31A1-KO SEM cells with (top) eGFP or SLC31A1 rescue, or (bottom) 100 μM $CuCl_2$ pre-treatment for 24 hours. $n = 4$ biological replicates (wells) for each condition are plotted per timepoint. Plotted data are mean ± SD, P values from two-sided Šídák's multiple comparisons test adjusted for multiple comparisons. Each dot represents a biological replicate. BCS and $CuCl_2$ were used at 50 μM. OE = overexpression, BCS = bathocuproinedisulfonic acid, oligo = oligomycin, AA = antimycin A, rot = rotenone, FCCP = carbonyl cyanide-p-trifluoromethoxyphenylhydrazone, perm = XF Plasma Membrane Permeabilizer, pyr/mal = pyruvate and malate, succ = succinate.

https://doi.org/10.1038/s43018-026-01177-4

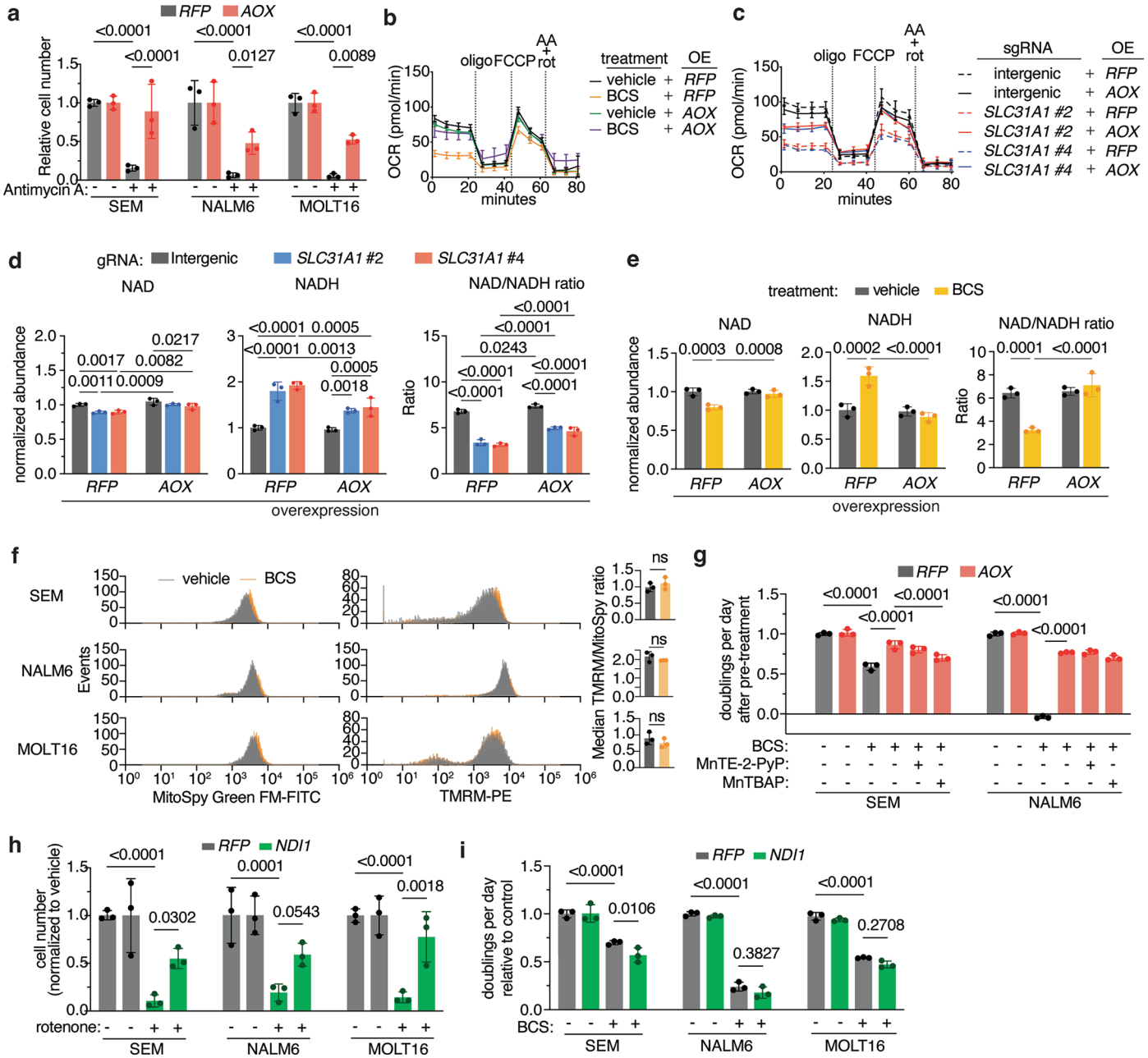

Extended Data Fig. 6 | Rescue of ETC activity with AOX over expression partially rescues cell proliferation in the context of copper depletion. (**a**) Relative cell number of SEM, NALM6 or MOLT16 cells expressing RFP or AOX and treated with vehicle or Antimycin A (5 nM) for 3 days. $n = 3$ biological replicates per condition. P values from two-sided Šídák's multiple comparisons test adjusted for multiple comparisons. (**b**-**c**) Seahorse MitoStress Assay on (**b**) 6-day BCS-treated SEM cells overexpressing RFP or AOX, or (**c**) SLC31A1-KO SEM cells overexpressing RFP or AOX. Plotted data are mean ± SD with 5 technical replicates (wells) for Seahorse Assays. (**d**-**e**) Levels of NAD, NADH and NAD/NADH ratio were determined by LC-MS targeted metabolite profiling in (**d**) SLC31A1-KO SEM cells over expressing RFP or AOX, or (**e**) day 8 BCS-treated SEM cells over expressing RFP or AOX. $n = 3$ biological replicates per condition. P values from two-sided Šídák's multiple comparisons test adjusted for multiple comparisons. (**f**) Flow cytometry histograms to measure mitochondrial mass (MitoSpy Green FM) and mitochondrial membrane potential (TMRM) in BCS-treated SEM (day 8), NALM6 (day 6), and MOLT16 (day 8) cells. Bar graphs depict the median TMRM/MitoSpy ratio for all recorded events. Cells were also gated for live cells using the Near IR Fixable LIVE/DEAD stain measured on the APC-Cy7 channel (APC-Cy7 negative). Combined data from 3 biological replicates per condition are shown in the histograms. (**g**) Doublings per day from day 5–11 of BCS-treated AOX-overexpressing SEM or NALM6 cells also treated with MnTE-2-PyP (20 μM) or MnTBAP (50 μM). $n = 3$ biological replicates. P values from two-sided Šídák's multiple comparisons test adjusted for multiple comparisons. (**h**) Relative cell number of SEM, NALM6, or MOLT16 cells expressing RFP or NDI1 and treated with vehicle or Antimycin A (5 nM) for 3 days. $n = 3$ biological replicates per condition. P values from two-sided Šídák's multiple comparisons test adjusted for multiple comparisons. (**i**) Doublings per day from day 5–11 of BCS treatment of SEM, NALM6, or MOLT16 cells overexpressing RFP or NDI1. $n = 3$ biological replicates per condition. P values from two-sided Šídák's multiple comparisons test adjusted for multiple comparisons. Plotted data are mean ± SD, P values from two-sided Šídák's multiple comparisons test adjusted for multiple comparisons. Each dot represents a biological replicate. oligo = oligomycin, AA = antimycin A, Rot = rotenone, FCCP = carbonyl cyanide-p-trifluoromethoxyphenylhydrazone, MnTE-2-PyP = manganese (III) meso-tetrakis (N-ethylpyridinium-2-yl) porphyrin, MnTBAP = manganese (III) tetrakis(4-benzoic acid) porphyrin chloride, AOX = alternative oxidase from Ciona intestinalis, NDI1 = yeast NADH-ubiquinone reductase, TMRM = tetramethylrhodamine methyl ester perchlorate.

https://doi.org/10.1038/s43018-026-01177-4

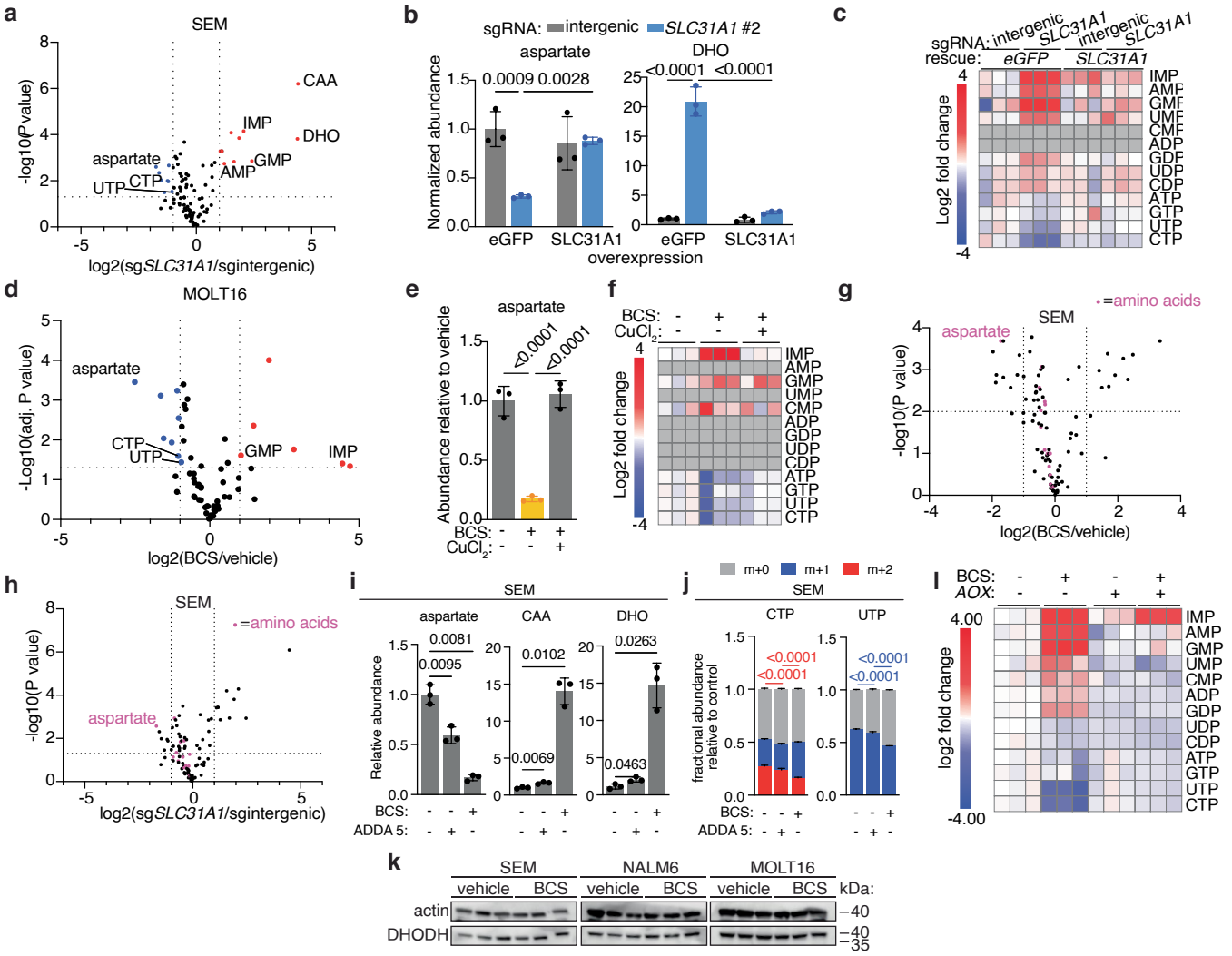

Extended Data Fig. 7 | See next page for caption.

https://doi.org/10.1038/s43018-026-01177-4

Extended Data Fig. 7 | Copper depletion disrupts nucleotide synthesis in an ETC-dependent manner. (**a**) Volcano plot of changing metabolites between SLC31A1-KO SEM cells and control cells. *n* = 3 biological replicates per condition. *P* values are from FDR-adjusted two-sided t-tests from MetaboAnalyst. (**b**) Aspartate and dihydroorotate (DHO) levels at baseline in SLC31A1-KO or control SEM cells with eGFP or SLC31A1 rescue. *n* = 3 biological replicates per condition. *P* values from two-sided Šídák's multiple comparisons test adjusted for multiple comparisons. (**c**) Nucleotide levels in SLC31A1-KO SEM cells with eGFP or SLC31A1 rescue. *n* = 3 biological replicates per condition. *P* values from two-sided Šídák's multiple comparisons test adjusted for multiple comparisons. (**d**) Volcano plot of changing metabolites between day 8 BCS-treated MOLT16 cells and control cells. *n* = 3 biological replicates per condition. *P* values are from FDR-adjusted two-sided t-tests from MetaboAnalyst. (**e-f**) Aspartate and nucleotide levels in day 8 BCS-treated MOLT16 cells. *n* = 3 biological replicates per condition. *P* values from two-sided Šídák's multiple comparisons test adjusted for multiple comparisons. (**g-h**) Volcano plot of significantly changing metabolites between day 14 BCS-treated (**g**) or SLC31A1-KO (**h**) SEM cells, with amino acids highlighted in pink. *n* = 3 biological replicates per condition. *P* values are from FDR-adjusted two-sided t-tests from MetaboAnalyst. (**i**) Relative abundance (normalized to vehicle-treated group) of aspartate, carbamoyl aspartic acid (CAA) or dihydroorotate (DHO) in SEM cells treated with BCS (8 days) or ADDA 5 (10 μM for 24 hours). Plotted data are mean ± SD. *n* = 3 biological replicates per condition, *P* values from two-sided Sidak's multiple comparison's test adjusted for multiple comparisons. (**j**) Fractional ^{15}N-glutamine label incorporation into CTP and UTP in 8-day BCS-treated SEM cells and SEM cells treated with 10 μM ADDA 5 for 24 h. *n* = 3 biological replicates per condition. Plotted data are mean ± SD. *P* values from two-sided Tukey's multiple comparisons test adjusted for multiple comparisons. (**k**) Western blot for DHODH levels in BCS-treated SEM (day 8), NALM6 (day 6) and MOLT16 cells (day 8); each lane represents an independent biological replicate. Actin is a loading control. (**l**) Nucleotide levels in AOX-overexpressing SEM cells treated with BCS for 8 days. *n* = 3 biological replicates per condition. *P* values from two-sided Šídák's multiple comparisons test adjusted for multiple comparisons. (**m-n**) Levels of aspartate, DHO, and IMP in (**m**) 14-day BCS-treated SEM cells overexpressing RFP or AOX, or (**n**) SLC31A1-KO SEM cells overexpressing RFP or AOX. *n* = 3 biological replicates per condition. *P* values from two-sided Šídák's multiple comparisons test adjusted for multiple comparisons. DHO = dihydroorotate, CAA = carbamoyl aspartic acid, AOX = alternative oxidase, IMP = inosine monophosphate. Plotted data are mean ± SD.

https://doi.org/10.1038/s43018-026-01177-4

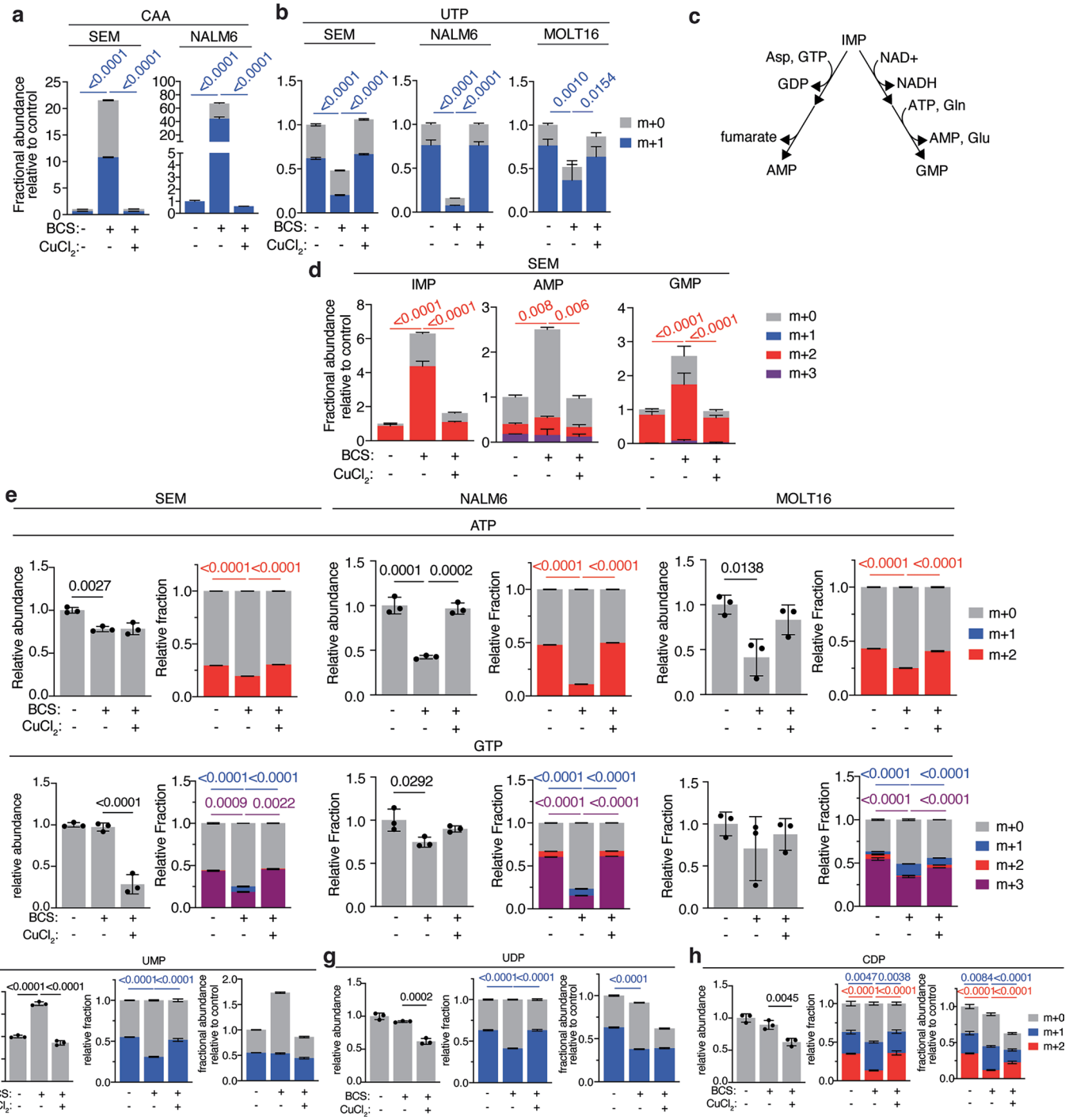

Extended Data Fig. 8 | Both purine and pyrimidine synthesis are impacted by copper depletion. (**a-b**) Fractional abundance of ^{15}N-labelled metabolites relative to levels in vehicle-treated cells in BCS-treated SEM cells (14 days), NALM6 (6 days) or MOLT16 (8 days). $n = 3$ biological replicates per condition. *P* values from two-sided Tukey's multiple comparisons test adjusted for multiple comparisons. (**c**) scheme of substrates consumed to synthesize adenosine monophosphate (AMP) and guanosine monophosphate (GMP) from inosine monophosphate (IMP). (**d**) Fractional abundance of ^{15}N-labelled purine monophosphates in 14-day BCS treated SEM cells relative to vehicle-treated cells. $n = 3$ biological replicates per condition. *P* values from two-sided Tukey's multiple comparisons test adjusted for multiple comparisons. (**e**) Relative abundance (normalized to vehicle-treated group) (left bar graphs) or fractional ^{15}N label incorporation (right bar graphs) of indicated metabolites in BCS-treated SEM (14 days), NALM6 (6 days) or MOLT16 (8 days) cells. $n = 3$ biological replicates per condition. (**f-h**) (left) Relative abundance (normalized to vehicle-treated group), (middle) fractional labelling, and (right) fractional abundance normalized to vehicle treated cells of ^{15}N label incorporation of indicated metabolites in 14-day BCS-treated SEM cells. $n = 3$ biological replicates per condition. All plotted data are mean ± SD. *P* values from two-sided Tukey's multiple comparisons test adjusted for multiple comparisons.

https://doi.org/10.1038/s43018-026-01177-4

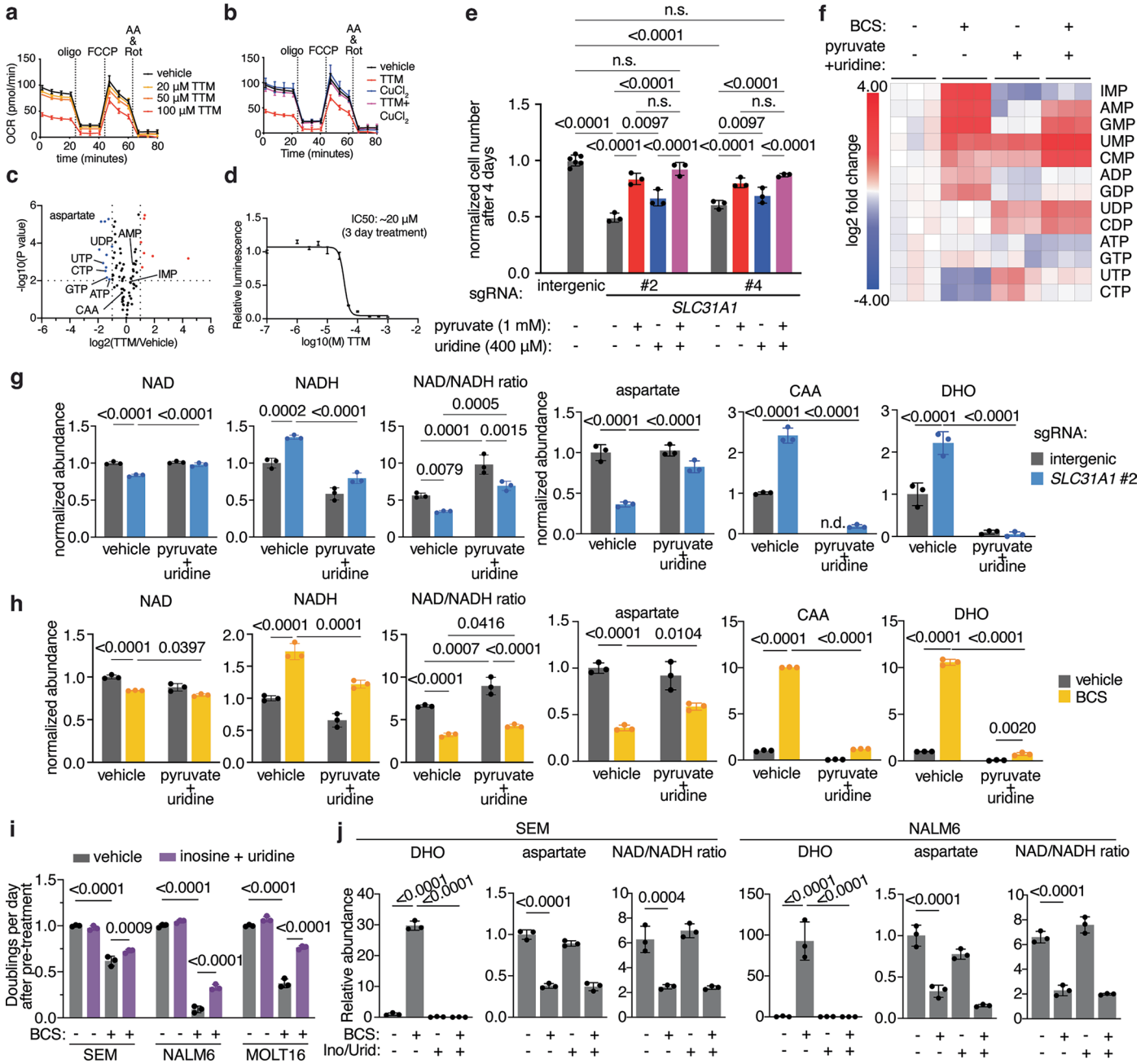

Extended Data Fig. 9 | Supplementation with nucleoside or nucleoside precursors bolsters nucleotide synthesis in copper-depleted cells. (**a**) MitoStress Seahorse assay of SEM cells treated for 24 hours with the indicated concentrations of TTM. $n = 4$ biological replicates (wells) per condition per timepoint. (**b**) MitoStress Seahorse assay of SEM cells treated with the indicated concentrations of TTM and/or $CuCl_2$ for 24 hours. $n = 4$ biological replicates (wells) per condition per timepoint. (**c**) Volcano plot of significantly changing metabolites determined by LC-MS targeted metabolite profiling in cells treated with TTM for 24 hours compared to vehicle treated cells. $n = 3$ biological replicates. *P* values are from FDR-adjusted two-tailed t-tests from MetaboAnalyst. (**d**) Cell-TiterGlo assay on SEM cells seeded at 0.25 million cells/mL and treated with varying concentrations of TTM for 3 days, with IC50 calculated using GraphPad Prism. Plotted data are mean ± SD of 5 technical replicates (wells) for both Seahorse and Cell-TiterGlo assays. M = molar. oligo = oligomycin, AA = antimycin A, rot = rotenone. (**e**) Cell number after 4 days of growth for SLC31A1-KO cells treated with pyruvate and/or uridine relative to vehicle-treated intergenic sgRNA-containing cells, all seeded at 0.1 million/mL. $n = 6$ (for intergenic) and 3 (for guides #2 and #4) biological replicates as indicated (each dot represents a different replicate), data is a combination of 2 independent experimental replicates using 2 different guides. *P* values from two-sided Šídák's multiple comparisons test adjusted for multiple comparisons. (**f**) Nucleotide levels in SEM cells treated with BCS and/or pyruvate and uridine for 8 days. $n = 3$ biological replicates per condition. *P* values from two-sided Šídák's multiple comparisons test adjusted for multiple comparisons. (**g-h**) Whole cell NAD, NADH and NADH ratios in (**c**) SLC31A1-KO SEM cells with or without pyruvate and uridine treatment, or (**d**) 14-day BCS-treated SEM cells with or without concurrent pyruvate and uridine treatment. $n = 3$ biological replicates per condition. *P* values from two-sided Šídák's multiple comparisons test adjusted for multiple comparisons. (**i**) Doublings per day from days 5–11 (SEM and NALM6) or days 2–8 (MOLT16) of cells treated with BCS and/or uridine and inosine (100 µM each). Doubling rate was calculated from the linear regression of cell number across at least 2 passages. $n = 3$ biological replicates per condition. *P* values from two-sided Šídák's multiple comparisons test adjusted for multiple comparisons. (**j**) Levels of dihydroorotate (DHO), aspartate, or the NAD/NADH ratio in SEM and NALM6 cells after 8 days of treatment with BCS and/or inosine and uridine (Ino/Urid) relative to vehicle treated cells. $n = 3$ biological replicates per condition. *P* values from two-sided Šídák's multiple comparisons test adjusted for multiple comparisons. CAA = carbamoyl aspartic acid. Plotted data are mean ± SD, *P* values from two-sided Šídák's multiple comparisons test adjusted for multiple comparisons. Each dot represents a biological replicate.

https://doi.org/10.1038/s43018-026-01177-4

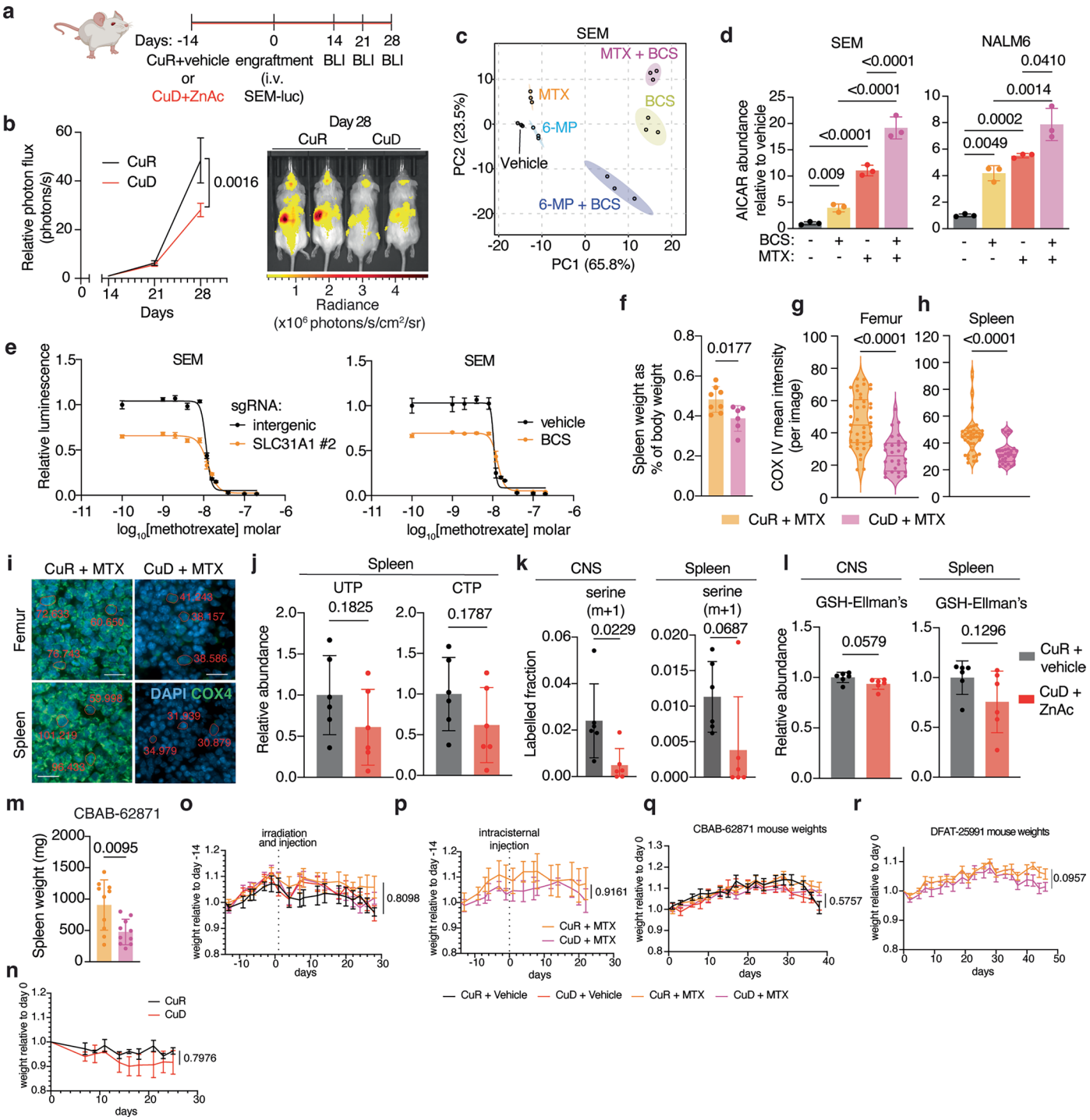

Extended Data Fig. 10 | See next page for caption.

https://doi.org/10.1038/s43018-026-01177-4

Extended Data Fig. 10 | Dietary copper depletion combines with methotrexate to reduce leukemic growth in vivo. (**a**) Experimental setup for copper depletion in leukemic mice. BLI = bioluminescent imaging. i.v. = intravenous. (**b**) Total photon flux from BLI at indicated timepoints expressed as fold change compared to day 14. *n* = 5 (CuR) or 6 (CuD) mice. Plotted values represent mean +/− SEM. Representative BLI images shown on the right. *P* value from two-sided Šídák's multiple comparisons test adjusted for multiple comparisons. (**c**) Principal component analysis (PCA) plot of targeted LC-MS metabolomics data of SEM cells. Cells were treated with 50 μM BCS for 8 days, 6-mercaptopurine (6-MP, 500 nM) for 24 hours, and/or methotrexate (MTX, 5 nM) for 24 hours. (**d**) Relative abundances of AICAR in MTX and BCS treated SEM and NALM6 cells, related to panel (**c**). *n* = 3 biological replicates per condition. *P* value from two-sided Šídák's multiple comparisons test adjusted for multiple comparisons. (**e**) Dose-responsive curves of either SLC31A1-KO SEM cells or 8-day BCS-treated SEM cells treated with MTX for 3 days. Cells were plated in 96-well plates at a density of 0.25 million/mL. Relative luminescence was measured as a proxy for cell number using CellTiter-Glo. *n* = 4 biological replicates (wells) per concentration of drug. (**f**) Spleen weights at day 30 of mice from Main Fig. 4c as a percentage of total body weight. *n* = 8 and 6 independent mice per group. *P* value from unpaired two-tailed t-tests. (**g-h**) Quantification of mean intensity value for COX IV staining per whole image using ZEN for mouse (**g**) femurs and (**h**) spleens. 4–6 images were quantified per tissue per mouse. For femurs, *n* = 41 and 28 total images and for spleens, *n* = 41 and 31 images were quantified respectively. Lines indicate quartiles and median. *P* value from unpaired two-tailed t-tests. (**i**) Example of per-cell quantification of COX IV staining intensity. Numbers in red indicate mean intensity value as reported from ZEN. All scale bars are 20 micrometers. (**j**) Relative unlabeled UTP and CTP levels in SEM leukemia cells harvested by MACS from the spleens of CuR+Vehicle or CuD+ZnAc treated mice. *n* = 6 independent mice per group. *P* value from unpaired two-tailed t-tests. (**k**) m + 1 ^{13}C-labelled fraction of serine as measured from SEM leukemia cells harvested from the CNS or spleens of mice by MACS. *n* = 6 independent mice per group. *P* value from unpaired two-tailed t-test. (**l**) Ellman's-derivatized glutathione (GSH) levels in SEM leukemia cells harvested from CNS or spleen. *n* = 6 independent mice per group. *P* value from unpaired two-tailed t-test. (**m**) Spleen weights from the endpoint of mice engrafted with PDX CBAB-62871 at week 7, related to Fig. 5m-n. *n* = 10 independent mice per group. *P* value from unpaired two-tailed t-test. (**n**) Mouse weights from experiment in Extended Data Fig. 10a, b. Plotted values are mean +/− SEM. *n* = 5 (CuR) or 6 (CuD) mice. *P* value from two-sided Sidak's multiple comparisons test adjusted for multiple comparisons, for day 25 CuR vs. CuD. (**o**) Mouse weights from experiment in Main Fig. 5b–d. Plotted values represent mean +/− SEM. *n* = 9 CuR+Vehicle, 8 CuD+Vehicle, 9 CuR+MTX, 6 CuD+MTX mice per group. *P* value from two-sided Tukey's multiple comparisons test adjusted for multiple comparisons for day 28 CuR+MTX vs. CuD+MTX. (**p**) Mouse weights from experiment in Main Fig. 5f–h. Plotted values represent mean +/− SEM. *n* = 10 mice per group. *P* value from two-sided Sidak's multiple comparisons test adjusted for multiple comparisons for day 22 CuR+MTX vs. CuD+MTX. (**q**) Mouse weights from experiment in Main Fig. 5m–n. Plotted values represent mean +/− SEM. *n* = 6 CuR+Vehicle, 5 CuD+Vehicle, 16 CuR+MTX, and 17 CuD+MTX mice from weeks 1–6. Combined data from two experimental replicates is shown; in the second replicate, mice were also measured at week 7 (*n* = 10 for CuR+MTX, *n* = 11 for CuD+MTX). Combined data from two experimental replicates is shown. *P* value from two-sided Tukey's multiple comparisons test adjusted for multiple comparisons, for day 38 CuR+MTX vs. CuD+MTX. (**r**) Mouse weights from experiment in Main Fig. 5o, p. Plotted values represent mean +/− SEM. *n* = 8 mice from week 4–6 and 5 mice per group at week 7. *P* value from two-sided Tukey's multiple comparisons test adjusted for multiple comparisons, for day 48 of CuR+MTX vs. CuD+MTX. n.s. = not significant. CuR = copper replete diet, CuD = copper depleted diet, AICAR = 5-aminoimidazole-4-carboxamide ribonucleotide, MACS = magnet-activated cell sorting. Plotted values are mean +/− SD unless otherwise specified. n.s. = not significant. *P* values from two-sided Šídák's multiple comparisons test adjusted for multiple comparisons (**b, d, n, p**), unpaired two-tailed t-tests (**f-h, j-m**) or Tukey's multiple comparisons test adjusted for multiple comparisons (**o, q-r**).

nature portfolio

Corresponding author(s): Naama Kanarek

Last updated by author(s): April 3, 2026

Reporting Summary

Nature Portfolio wishes to improve the reproducibility of the work that we publish. This form provides structure for consistency and transparency in reporting. For further information on Nature Portfolio policies, see our Editorial Policies and the Editorial Policy Checklist.

Statistics

For all statistical analyses, confirm that the following items are present in the figure legend, table legend, main text, or Methods section.

n/a	Confirmed
☐	☒ The exact sample size (*n*) for each experimental group/condition, given as a discrete number and unit of measurement
☐	☒ A statement on whether measurements were taken from distinct samples or whether the same sample was measured repeatedly
☐	☒ The statistical test(s) used AND whether they are one- or two-sided *Only common tests should be described solely by name; describe more complex techniques in the Methods section.*
☐	☒ A description of all covariates tested
☐	☒ A description of any assumptions or corrections, such as tests of normality and adjustment for multiple comparisons
☐	☒ A full description of the statistical parameters including central tendency (e.g. means) or other basic estimates (e.g. regression coefficient) AND variation (e.g. standard deviation) or associated estimates of uncertainty (e.g. confidence intervals)
☐	☒ For null hypothesis testing, the test statistic (e.g. *F*, *t*, *r*) with confidence intervals, effect sizes, degrees of freedom and *P* value noted *Give P values as exact values whenever suitable.*
☒	☐ For Bayesian analysis, information on the choice of priors and Markov chain Monte Carlo settings
☒	☐ For hierarchical and complex designs, identification of the appropriate level for tests and full reporting of outcomes
☐	☒ Estimates of effect sizes (e.g. Cohen's *d*, Pearson's *r*), indicating how they were calculated

Our web collection on statistics for biologists contains articles on many of the points above.

Software and code

Policy information about availability of computer code

Data collection	BD FACSDIVA (v.8.0.1), ZEN (v3.11), LivingImage (v4.8.2), BD FACS Chorus (v.3.0)
Data analysis	Prism (v10), FlowJo (v10 and v11), TraceFinder (v4.1), CompoundDiscoverer (v3.3), IsoCorrectoR. R scripts used for formatting and normalization of metabolomics datasets can be found at: https://github.com/FrozenGas/KanarekLabTraceFinderRScripts.

For manuscripts utilizing custom algorithms or software that are central to the research but not yet described in published literature, software must be made available to editors and reviewers. We strongly encourage code deposition in a community repository (e.g. GitHub). See the Nature Portfolio guidelines for submitting code & software for further information.

Data

Policy information about availability of data

All manuscripts must include a data availability statement. This statement should provide the following information, where applicable:

- Accession codes, unique identifiers, or web links for publicly available datasets
- A description of any restrictions on data availability
- For clinical datasets or third party data, please ensure that the statement adheres to our policy

NGS data for the barcoding experiment and in vivo CRISPR screen are deposited in the SRA (BioSample accessions: SAMN57078993, SAMN57078994) and are available in the supplementary datasets. All metabolomics data are available at the NIH Common Fund's National Metabolomics Data Repository (NMDR) website, the Metabolomics Workbench, https://www.metabolomicsworkbench.org where it has been assigned Project ID (PR002390). The data can be accessed directly via

it's Project DOI 10.21228/M8Q250. This work is supported by Metabolomics Workbench/National Metabolomics Data Repository (NMDR) (grant# U2C-DK119886), Common Fund Data Ecosystem (CFDE) (grant# 3OT2OD030544) and Metabolomics Consortium Coordinating Center (M3C) (grant# 1U2C-DK119889). Data for survival analyses was obtained from the NIH GDC: https://portal.gdc.cancer.gov/projects/TARGET-ALL-P2, https://portal.gdc.cancer.gov/projects/MP2PRT-ALL and from Xena (https://xenabrowser.net/). Other data and materials that support the findings of this study are available from the corresponding author upon request

Research involving human participants, their data, or biological material

Policy information about studies with human participants or human data. See also policy information about sex, gender (identity/presentation), and sexual orientation and race, ethnicity and racism.

Reporting on sex and gender	Sex, genotypic info and relevant clinical data for the 2 PDXs used are provided in Supplementary Table S2.
Reporting on race, ethnicity, or other socially relevant groupings	N/A
Population characteristics	Sex, genotypic info and relevant clinical data for the 2 PDXs used are provided in Supplementary Table S2.
Recruitment	PDXs were obtained under MTA from the Public Repository of Xenografts (ProXE https://www.proxe.org/).
Ethics oversight	PDXs were obtained under MTA from the Public Repository of Xenografts (ProXE https://www.proxe.org/).

Note that full information on the approval of the study protocol must also be provided in the manuscript.

Field-specific reporting

Please select the one below that is the best fit for your research. If you are not sure, read the appropriate sections before making your selection.

☒ Life sciences ☐ Behavioural & social sciences ☐ Ecological, evolutionary & environmental sciences

For a reference copy of the document with all sections, see nature.com/documents/nr-reporting-summary-flat.pdf

Life sciences study design

All studies must disclose on these points even when the disclosure is negative.

Sample size	No sample size calculations were performed a priori. Sample sizes were based on what has been the standard in the field (3-5 for in vitro assays including Seahorse assay, and 6-12 for in vivo assays), see Kanarek et al., 2018 in Nature, Martinez-Reyes et al., 2020 in Nature.
Data exclusions	For Seahorse data, wells were excluded if values did not show response to injected drugs compared to the others within the same group. This exclusion criteria was pre-established to address technical noise due to improper loading of wells or injection port failure.
Replication	Data from all replicates from all experiments is included in the paper as discussed in the figure legends. All replicates of presented experiments display were concordant with the presented results.
Randomization	For all in vitro experiments, cells treatments were administered randomly. For mouse experiments, mice were randomized into groups such that each cage contained members of both groups, and that each group contained mixed sexes. Randomization was performed while ensuring equal group size and even distribution of mice from both sexes in all treatment groups. If IVIS data was available, mice were randomized to groups based on IVIS leukemia burden; otherwise, mice were randomized to groups by cage such that each group was represented in each cage.
Blinding	Experimenters were not blinded to groups in vitro experiments during data collection as this was not feasible due to the administration of treatments and labelling of flasks and cell culture dishes. Experimenters were not blinded to groups during mouse weight monitoring or IVIS, since cages were visually distinguishable in by diets and drinking water treatments. During FACS monitoring of PDX progression, experimenters were blinded to treatment group and only after final analysis using FlowJo was the data re-linked to the experimental groups. During Tracefinder analysis, experimenters were blinded to the experimental groups. For histology, experimenters were blinded to the groups until final data aggregation and statistical testing.

Reporting for specific materials, systems and methods

We require information from authors about some types of materials, experimental systems and methods used in many studies. Here, indicate whether each material, system or method listed is relevant to your study. If you are not sure if a list item applies to your research, read the appropriate section before selecting a response.

Materials & experimental systems

n/a	Involved in the study
☐	☒ Antibodies
☐	☒ Eukaryotic cell lines
☒	☐ Palaeontology and archaeology
☐	☒ Animals and other organisms
☒	☐ Clinical data
☒	☐ Dual use research of concern
☒	☐ Plants

Methods

n/a	Involved in the study
☒	☐ ChIP-seq
☐	☒ Flow cytometry
☒	☐ MRI-based neuroimaging

Antibodies

Antibodies used

Antibodies

For reducing and denaturing western blot:
vinculin (CST 13901; 1:2500)
Beta actin (CST 8457; 1:2000)
GAPDH (CST 2118L; 1:2000)
MT-CO1/COX1 (abcam ab14705; 1:2000)
COX4I1/COX4 (CST 4850; 1:1000)
COX2 (Proteintech 55070-1-AP; 1:5000)
DHODH (Santa Cruz E-8 sc-166348; 1:500)
SDHA (CST 5839S; 1:1000)
SLC31A1 (CST 13086S; 1:500)
Beta tubulin (CST 2128P; 1:1000)
Human Total OxPhos Cocktail (abcam ab110411; 1:1000)
VDAC1/porin (abcam ab154856; 1:1000)
Total ERK1/2 (CST 4696S; 1:1000)
Phospho-ERK1/2 (CST 4370L; 1:1000)

Primary antibodies were diluted in Signal Enhancer HIKARI Solution 1 (Nacalai USA NU00102).

For blue-native PAGE, the following antibodies were used:
MT-CO1/COX1 (ABCAM, ab14705, 1:2000)
SDHA (Santa Cruz, sc-166947,1:20,000)
NDUFS1 (Abcam, ab169540,1:1000)
UQCR4/CYC1 (Millipore Sigma, HPA001247,1:2000)

Secondary antibodies used were:
Peroxidase AffiniPure Goat Anti-Mouse IgG H+L (Jackson ImmunoResearch Laboratories, #115-035-166) and Peroxidase AffiniPure Goat Anti-Rabbit IgG H+L (Jackson ImmunoResearch Laboratories, #111-035-144) were both diluted 1:10,000 in 5% milk in TBST and incubated with immunoblots for 1 hour at room temperature.

For flow sorting of SLC31A1-stained cells:
Anti-SLC31A1/CTR1 antibody (Abcam AB129067))
Donkey anti-Rabbit secondary antibody (PE – BioLegend 406414, or Alexa 647 – Biolegend 406421)

For mouse in vivo mixing experiments and PDX experiments:
Anti-human CD19 – Pacific Blue (Biolegend 302223)
Anti-human CD45 – PE (BioLegend 304008)
Anti-human CD2 – FITC (BioLegend 984902)
Fixable Near IR Live-Dead Stain (Thermo L10119)

Validation

All antibodies were available commercially and validated by their respective companies. For SLC31A1 indirect staining by flow cytometry, specificity of the staining was confirmed in-house by comparing SLC31A1-KO and overexpression cells (see Extended Data Fig 2B-C); the MFI of these cells correlated well with their expected SLC31A1 status.

Eukaryotic cell lines

Policy information about cell lines and Sex and Gender in Research

Cell line source(s)

The sources of the cell lines are as follows: SEM, NALM-6: D. M. Sabatini, Massachusetts Institute of Technology (MIT); MOLT4, MOLT16, PF382, REH: A. Gutierrez, Dana-Farber Cancer Institute.

Authentication

Cell lines were validated using STR profiling at the DFCI Molecular Diagnostics Core in Dec 2022 prior to use.

Mycoplasma contamination	All cell lines were tested monthly for mycoplasma by PCR.
Commonly misidentified lines (See ICLAC register)	N/A

Animals and other research organisms

Policy information about studies involving animals; ARRIVE guidelines recommended for reporting animal research, and Sex and Gender in Research

Laboratory animals	All mice used were mixed sex NOD.CB17-Prkdcscid/NCrCrl (originally purchased from Charles River and maintained at the BCH ARCH animal facility by self-breeding), and 5-12 weeks of age at the start of each experiment.
Wild animals	N/A
Reporting on sex	All mice used were mixed sex; for treatment studies, mice were randomized to have equal number and equal representation of mice in each group (approximately 2:1 female:male, due to the observed female-biased litters in our colony). At least 2 females and 2 males were included at the start of every experiment.
Field-collected samples	N/A
Ethics oversight	The Committee for Animal Care at Boston Children's Hospital approved all animal procedures carried out in this study.

Note that full information on the approval of the study protocol must also be provided in the manuscript.

Plants

Seed stocks	*Report on the source of all seed stocks or other plant material used. If applicable, state the seed stock centre and catalogue number. If plant specimens were collected from the field, describe the collection location, date and sampling procedures.*
Novel plant genotypes	*Describe the methods by which all novel plant genotypes were produced. This includes those generated by transgenic approaches, gene editing, chemical/radiation-based mutagenesis and hybridization. For transgenic lines, describe the transformation method, the number of independent lines analyzed and the generation upon which experiments were performed. For gene-edited lines, describe the editor used, the endogenous sequence targeted for editing, the targeting guide RNA sequence (if applicable) and how the editor was applied.*
Authentication	*Describe any authentication procedures for each seed stock used or novel genotype generated. Describe any experiments used to assess the effect of a mutation and, where applicable, how potential secondary effects (e.g. second site T-DNA insertions, mosiacism, off-target gene editing) were examined.*

Flow Cytometry

Plots

Confirm that:

☒ The axis labels state the marker and fluorochrome used (e.g. CD4-FITC).

☒ The axis scales are clearly visible. Include numbers along axes only for bottom left plot of group (a 'group' is an analysis of identical markers).

☒ All plots are contour plots with outliers or pseudocolor plots.

☒ A numerical value for number of cells or percentage (with statistics) is provided.

Methodology

Sample preparation	Flow cytometry was performed on a BD Fortessa and flow sorting was performed on a BD FACSMelody. Briefly, for samples from cell culture or from mice, cells were washed with fluorescence-activated cell sorting (FACS) buffer (PBS + 2% FBS + 2 uM EDTA) and incubated for 30 min in the presence of the indicated antibodies and live/dead stains on ice. After staining, cells were washed once with FACS buffer and then analyzed on ice. For staining SLC31A1 by indirect staining, cells were washed with FACS buffer and then incubated for 30 min with the primary antibody (Abcam AB129067). The cells were then spun down, washed once with FACS buffer, then incubated for 30 min with PE or Alexa 647 secondary antibody (BioLegend 406414 or 406421). For cell sorting, all staining steps and the sorting procedure itself was performed at room temperature to preserve cell viability. For in vivo mixing experiments, SEM cells were distinguished from murine cells by GFP/mCherry expression as well as human CD19+ staining. The following flow cytometry antibodies were used: For flow sorting of SLC31A1-stained cells: Anti-SLC31A1/CTR1 antibody (Abcam AB129067)) Donkey anti-Rabbit secondary antibody (PE – BioLegend 406414, or Alexa 647 – Biolegend 406421) For mouse in vivo mixing experiments and PDX experiments: Anti-human CD19 – Pacific Blue (Biolegend 302223)

	Anti-human CD45 – PE (BioLegend 304008) Anti-human CD2 – FITC (BioLegend 984902) Fixable Near IR Live-Dead Stain (Thermo L10119)
Instrument	Flow cytometry was performed on a BD Fortessa and flow sorting was performed on a BD FACSMelody.
Software	BD DIVA 8.2 (Fortessa), FACSChorus (Melody)
Cell population abundance	Purity of post-sort fractions is depicted in the Extended Data.
Gating strategy	Relevant gating strategies are depicted in the Extended Data.

☒ Tick this box to confirm that a figure exemplifying the gating strategy is provided in the Supplementary Information.